to the anomeric hydrogen. In contrast, the glycosidic torsion angles in the branched sialosides are around -160° and -15°, and the aglycon is placed anti to the anomeric carboxylate substituent. The driving force for the anti orientation is believed to result from the bulky and extensively solvated carboxylate group at the anomeric center, which forces the other bulky substituent aglycon into the least hindered position. This orientation, however, is in accord with the exoanomeric effect. In contrast to the rigidity of the branched sialosides, the terminal sialosides appear to be more flexible. The observed differences between the hydrogen

and carbon T_1 values reported in Table I for the branched and linear sialoside residues are in accord with these conclusions. Thus, the experimental results together with the HSEA calculations reported in this paper provide a good structural model for the hexasaccharide of ganglioside GD1a.

An Electronic Structural Comparison of Copper–Peroxide Complexes of Relevance to Hemocyanin and Tyrosinase Active Sites

Paul K. Ross and Edward I. Solomon*

Contribution from the Department of Chemistry, Stanford University, Stanford, California 94305. Received August 22, 1990

Abstract: Self-consistent field-$X\alpha$-scattered wave (SCF-$X\alpha$-SW) calculations have been performed on a series of copper(II) peroxide structures to evaluate the effects of peroxide bridging geometry on the electronic structure and bonding. The series of structures investigated allows comparison of a set of copper–peroxide monomers and dimers with different binding geometries but with similar ligand environments. The Cu–O and O–O bonding interactions, magnetic exchange interactions, and excited-state transition energies are calculated and compared to experimental properties of structurally related analogues. The primary bonding interaction in all structures involves the in-plane peroxide Π^*_σ orbital bonding with the Cu d ground-state orbitals. The side-on dimer has an additional bonding interaction where the peroxide σ^* orbital acts as a π-acceptor, weakening the O–O bond, consistent with the observed low stretching frequency. The energy difference between the in-plane peroxide Π^*_σ and the out-of-plane peroxide Π^*_v orbitals is related to the strength of the copper–peroxide bond and is a measure of the stability of the copper–peroxide adduct. The Π^*_v–Π^*_σ splitting of the side-on dimer is significantly larger than other geometries and is consistent with the observed absorption spectrum. Finally, the electronic structure origin of proposed reaction mechanisms is discussed, and models of relevance to oxyhemocyanin and oxytyrosinase are evaluated.

The ability of copper-containing metalloproteins to reversibly bind and react with dioxygen has been of continued interest in bioinorganic chemistry.[1-5,8] Hemocyanin, tyrosinase, and multicopper oxidases such as laccase, ascorbate oxidase, and ceruloplasmin are examples of metalloproteins that contain copper and interact with dioxygen. Hemocyanin, the oxygen transport protein in arthropods and molluscs, contains a coupled binuclear copper active site which reversibly binds dioxygen as peroxide bridging between the two copper ions.[1] Tyrosinase contains a similar active site and catalyzes the orthohydroxylation of phenols with further oxidation of the catechol product to an *o*-quinone.[1,2] In addition to the coupled binuclear site, the multicopper oxidases also contain additional copper sites. In laccase and ascorbate oxidase there exists a trinuclear copper cluster which is involved in the reduction of dioxygen to water.[3] Understanding the reactivity of these systems requires a detailed knowledge of their electronic structure and that of copper–peroxide complexes in general.

The oxygenated forms of hemocyanin and tyrosinase are the only well-characterized copper–peroxide metalloprotein systems, although oxygen intermediates are known to exist in multicopper oxidases.[4] The active site of oxyhemocyanin contains two tetragonal copper(II) ions separated by 3.6 Å with dioxygen bound as peroxide bridging between the copper ions.[5] Resonance Raman data indicate that the peroxide is symmetrically bound between the copper ions and has a low O–O stretching frequency of 750 cm^{-1}.[6] In addition, oxyhemocyanin is diamagnetic and is not

detectable by electron paramagnetic resonance, indicating that the two copper(II) ions are strongly antiferromagnetically coupled $(-2J \geq 550$ cm^{-1} for H $= -2JS_1 \cdot S_2)$.[7] Oxyhemocyanin exhibits a unique absorption spectrum with an intense band at 580 nm $(\epsilon \sim 1000$ M^{-1} cm$^{-1})$ and an extremely intense band at 345 nm $(\epsilon \sim 20\,000$ M^{-1} cm$^{-1})$, which have been interpreted as peroxide to Cu(II) charge-transfer transitions of a symmetric bridging peroxide.[5] On the basis of studies of oxyhemocyanin and the met

(1) (a) Solomon, E. I.; Penfield, K. W.; Wilcox, D. E. *Struct. Bonding (Berlin)* **1983,** *53,* 1. (b) Solomon, E. I. *Pure Appl. Chem.* **1983,** *55,* 1069-1088. (c) Solomon, E. I. In *Copper Proteins;* Spiro, T. G., Ed.; Wiley: New York, 1981; p 41-108.

(2) Lerch, K. *Met. Ions Biol. Syst.* **1981,** *13,* 143-186.

(3) (a) Spira-Solomon, D. S.; Allendorf, M. D.; Solomon, E. I. *J. Am. Chem. Soc.* **1986,** *108,* 5319-5328. (b) Messerschmidt, A.; Rossi, A.; Ladenstein, R.; Huber, R.; Bolognesi, M.; Gatti, G.; Marchesini, A.; Petruzzelli, R.; Finazzi-Argo, A. *J. Mol. Biol.* **1989,** *206,* 513-529.

(4) (a) Andreasson, L. E.; Branden, R.; Malmstrom, B. G.; Vanngard, T. *FEBS Lett.* **1973,** *32,* 187-189. (b) Andreasson, L. E.; Branden, R.; Reinhammer, B. *Biochim. Biophys. Acta* **1976,** *438,* 370-379. (c) Aasa, R.; Branden, R.; Deinum, J.; Malmstrom, B. G.; Reinhammer, B.; Vanngard, T. *FEBS Lett.* **1976,** *61,* 115-119. (d) Aasa, R.; Branden, R.; Deinum, J.; Malmstrom, B. G.; Reinhammer, B.; Vanngard, T. *Biochem. Biophys. Res. Commun.* **1976,** *70,* 1204-1209. (e) Cole, J. L.; Tan, G. O.; Yang, E. K.; Hodgson, K. O.; Solomon, E. I. *J. Am. Chem. Soc.* **1990,** *112,* 2243-2249.

(5) Eickman, N. C.; Himmelwright, R. S.; Solomon, E. I. *Proc. Natl. Acad. Sci. U.S.A.* **1979,** *76,* 2094-2098.

(6) (a) Larrabee, J. A.; Spiro, T. G. *J. Am. Chem. Soc.* **1980,** *102,* 4217-4223. (b) Freedman, T. B.; Loehr, J. S.; Loehr, T. M. *J. Am. Chem. Soc.* **1976,** *98,* 2809-2815.

(7) Dooley, D. M.; Scott, R. A.; Ellinghaus, J.; Solomon, E. I.; Gray, H. B. *Proc. Natl. Acad. Sci. U.S.A.* **1978,** *75,* 3019-3022.

* Author to whom correspondence should be addressed.

Copper-Peroxide Complexes

J. Am. Chem. Soc., Vol. 113, No. 9, 1991 3247

azide hemocyanin derivative,[8] which contains azide bound to the two copper(II) ions, a spectroscopically effective model for the active site of oxyhemocyanin has been developed.[5,9] In this model the two coppers are bridged by peroxide in an end-on cis μ-1,2 configuration and by a second endogenous ligand, likely hydroxide.

In recent years, several small-molecule binuclear copper complexes that bind dioxygen have been synthesized and can serve as models for the coupled binuclear copper active site of hemocyanin and tyrosinase.[10-14] Spectroscopic studies of these analogues indicate that peroxide can bind in several different geometries and exhibit widely different absorption spectra. In particular, a recent structural characterization of the first side-on μ-η^2:η^2 peroxide bridged transition-metal dimer, [Cu(HB(3,5-iPr$_2$pz)$_3$]$_2$(O$_2$), exhibits a low O–O stretching frequency of 741 cm^{-1} and an absorption spectrum very similar to oxyhemocyanin and provides an alternative possibility for the structure of its active site.[10] In contrast, the only other structurally characterized copper–peroxide complex, [(CuL)$_2$(O$_2$)]$^{2+}$, has a copper–copper distance of 4.36 Å, an end-on trans μ-1,2 peroxide bridging geometry, an O–O stretching frequency of 832 cm^{-1}, and an absorption spectrum which is quite different from that of oxyhemocyanin.[11] Both of these dimers are bridged solely by peroxide and are strongly antiferromagnetically coupled, indicating that peroxide is an effective mediator of superexchange interactions. Resonance Raman data on another copper–peroxide complex,[12] [Cu$_2$(XYL–O–)O$_2$]$^{1+}$, which has been extensively studied but has not been crystallized, indicate that the peroxide is bound asymmetrically to only one copper with a possible weak axial interaction with a second copper and has an O–O stretching frequency of 803 cm^{-1}.[15] This complex provides a good model of a terminally bound peroxide to a copper(II) monomer.

The electronic structure and bonding in these copper–peroxide complexes have been qualitatively explained by using the following simple molecular orbital model which involves the highest occupied levels of the copper and the peroxide. When peroxide binds to a single copper(II) ion, the doubly degenerate, highest occupied Π^* molecular orbital of the peroxide splits into two nondegenerate levels designated Π^*_v and Π^*_σ. The Π^*_v orbital is oriented vertical to the Cu–O–O plane and only has a weak π interaction with the copper. The Π^*_σ orbital lies in the Cu–O–O plane and is σ bonding with respect to the copper. Due to the stronger bonding interaction of the Π^*_σ level, peroxide-to-copper charge-transfer transitions from this level are expected to be at higher energy and more intense than transitions from the Π^*_v level. The absorption spectrum of the monomer analogue, [Cu$_2$(XYL–O–)O$_2$]$^{1+}$, contains two intense bands at 625 ($\epsilon \sim 1100$ M^{-1} cm^{-1}) and 503 nm ($\epsilon \sim 6300$ M^{-1} cm^{-1}) which have been assigned respectively as the Π^*_v and Π^*_σ peroxide-to-copper charge-transfer transitions.[12] The Π^*_σ level is stabilized by 4000 cm^{-1} with respect to the Π^*_v, indicative of the strength of the Cu–O bond. When peroxide

end-on monomer, 1

end-on *trans* dimer, 2

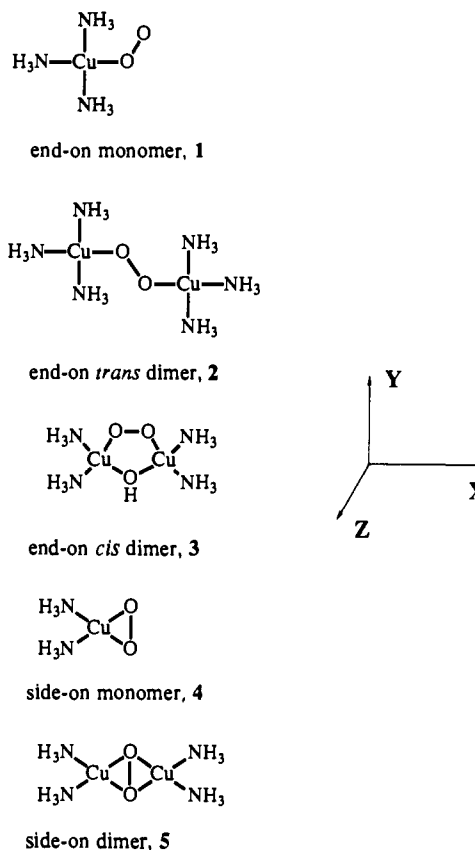end-on *cis* dimer, 3

side-on monomer, 4

side-on dimer, 5

Figure 1. Orientation of the molecular structures for **1–5** with respect to the molecular axes used in the calculations. All orbital descriptions are given with respect to these axes.

bridges between two copper(II) ions in a planar geometry, the highest occupied degenerate peroxide Π^* level will again split into Π^*_v and Π^*_σ levels. The two intense bands in the absorption spectrum of oxyhemocyanin have been assigned as Π^*_v (580 nm, $\epsilon \sim 1000$ M^{-1} cm^{-1}) and Π^*_σ (345 nm, $\epsilon \sim 20\,000$ M^{-1} cm^{-1}) charge-transfer transitions.[5] The additional bonding interaction due to the second copper in the active site further stabilizes the Π^*_σ level, resulting in a larger Π^*_v–Π^*_σ splitting of 12 000 cm^{-1}.

More detailed descriptions of the electronic structure of transition-metal complexes can be obtained through self-consistent field-Xα-scattered wave (SCF-Xα-SW) calculations.[16] The broken-symmetry Xα or Xα–valence bond (Xα–VB) procedure of Noodleman incorporates valence bond concepts into the Xα formalism and allows transition-metal dimers to be treated as two weakly interacting antiferromagnetically coupled monomers.[17] This formalism has been effectively applied to the binuclear iron-sulfur proteins[18] and has been extended to the 3-Fe[19] and 4-Fe clusters[20] and even to clusters involving different types of transition metals.[21] The broken-symmetry Xα (Xα–VB) for-

(8) (a) Pate, J. E.; Ross, P. K.; Thamann, T. J.; Reed, C. A.; Karlin, K. D.; Sorrel, T. N.; Solomon, E. I. *J. Am. Chem. Soc.* **1989**, *111*, 5198–5209. (b) Himmelwright, R. S.; Eickman, N. C.; Lubien, C. D.; Solomon, E. I. *J. Am. Chem. Soc.* **1980**, *102*, 5378–5388.

(9) Solomon, E. I. In *Metal Clusters in Proteins*; Que, L., Jr., Ed.; ACS Symposium Series 372; American Chemical Society: Washington, DC, 1988; pp 116–149.

(10) The ligand HB(3,5-iPr$_2$pz)$_3$ is hydridotris(3,5-diisopropylpyrazolyl)-borate. (a) Kitajima, N.; Fujisama, K.; Moro-oka, Y.; Toriumi, K. *J. Am. Chem. Soc.* **1989**, *111*, 8975–8976. (b) Kitajima, N.; Koda, T.; Hashimoto, S.; Kitagawa, T.; Moro-oka, Y. *J. Chem. Soc., Chem. Commun.* **1988**, 151–152.

(11) The ligand L is tris[(2-pyridyl)methyl]amine. Jacobson, R. R.; Tyeklar, Z.; Farooq, A.; Karlin, K. D.; Liu, S.; Zubieta, J. *J. Am. Chem. Soc.* **1988**, *110*, 3690–3692.

(12) The ligand XYL–O– contains two tridentate bis(2-pyridylethyl)amine donor units connected by 2-hydroxo-*m*-xylyl. (a) Karlin, K. D.; Cruse, R. W.; Gultneh, Y.; Farooq, A.; Hayes, J. C.; Zubieta, J. *J. Am. Chem. Soc.* **1987**, *109*, 2668–2679. (b) Karlin, K. D.; Cruse, R. W.; Gultneh, Y.; Hayes, J. C.; Zubieta, J. *J. Am. Chem. Soc.* **1984**, *106*, 3372–3374.

(13) Sorrell, T. N.; Vankai, V. A. *Inorg. Chem.* **1990**, *29*, 1687–1692.

(14) (a) Thompson, J. S. *J. Am. Chem. Soc.* **1984**, *106*, 4057–4059. (b) Thompson, J. S. *J. Am. Chem. Soc.* **1984**, *106*, 8308–8309.

(15) Pate, J. E.; Cruse, R. W.; Karlin, K. D.; Solomon, E. I. *J. Am. Chem. Soc.* **1987**, *109*, 2624–2630.

(16) (a) Slater, J. C. *Adv. Quantum Chem.* **1972**, *6*, 1–92. (b) Johnson, K. H. *Adv. Quantum Chem.* **1973**, *7*, 143–185. (c) Case, D. A. *Annu. Rev. Phys. Chem.* **1982**, *33*, 151–171. (d) Johnson, K. H. *Annu. Rev. Phys. Chem.* **1975**, *26*, 39–42. (e) Connolly, J. W. D. In *Semiempirical Methods of Electronic Structure Calculation, Part A: Techniques*; Segal, G. A., Ed.; Plenum: New York, 1977; pp 105–132. (f) Johnson, K. H.; Norman, J. G., Jr.; Connolly, J. W. D. In *Computational Methods for Large Molecules and Localized States in Solids*; Herman, F., McLean, A. D., Nesbet, R. K., Eds.; Plenum: New York, 1973; pp 161–201. (g) Cook, M. R. Ph.D. Thesis, Harvard University, 1981.

(17) (a) Noodleman, L.; Norman, J. G., Jr. *J. Chem. Phys.* **1979**, *70*, 4903–4906. (b) Noodleman, L. *J. Chem. Phys.* **1981**, *74*, 5737–5743.

(18) (a) Noodleman, L.; Baerends, E. J. *J. Am. Chem. Soc.* **1984**, *106*, 2316–2327. (b) Norman, J. G., Jr.; Ryan, P. B.; Noodleman, L. *J. Am. Chem. Soc.* **1980**, *102*, 4279–4282.

(19) Noodleman, L.; Case, D. A.; Aizman, A. *J. Am. Chem. Soc.* **1988**, *110*, 1001–1005.

(20) (a) Aizman, A.; Case, D. A. *J. Am. Chem. Soc.* **1982**, *104*, 3269–3279. (b) Noodleman, L.; Norman, J. G., Jr.; Osborne, J. H.; Aizman, A.; Case, D. A. *J. Am. Chem. Soc.* **1985**, *107*, 3418–3426.

Table I. Input Parameters for Calculations[a]

atom	x	y	z	radius	α	atom	x	y	z	radius	α
				A. $(NH_3)_3CuO_2$ (1)							
outer sphere	0.0000	0.0000	0.0000	6.8811	0.774 28	H1A	-1.7817	4.4094	0.0000	1.1700	0.978 04
Cu	0.0000	0.0000	0.0000	2.9500	0.706 97	H1B	0.8908	4.4094	±1.5430	1.1700	0.978 04
O1	3.4960	0.0000	0.0000	1.8400	0.744 47	H2A	-4.4094	-1.7817	0.0000	1.1700	0.978 04
O2	4.3234	2.5924	0.0000	1.8400	0.744 47	H2B	-4.4094	0.8908	±1.5430	1.1700	0.978 04
N1	0.0000	3.7795	0.0000	1.7000	0.751 97	H3A	1.7817	-4.4094	0.0000	1.1700	0.978 04
N2	-3.7795	0.0000	0.0000	1.7000	0.751 97	H3B	-0.8908	-4.4094	±1.5430	1.1700	0.978 04
N3	0.0000	-3.7795	0.0000	1.1700	0.751 97						
				B. $[(NH_3)_3CuO_2Cu(NH_3)_3]^{2+}$ (2)							
outer sphere	0.0000	0.0000	0.0000	9.9090	0.786 57	H1B	-3.0189	5.7056	±1.5430	1.1700	0.978 04
Cu1	-3.9097	1.2962	0.0000	2.9500	0.706 97	H2A	-8.3191	-0.4855	0.0000	1.1700	0.978 04
Cu2	3.9097	-1.2962	0.0000	2.9500	0.706 97	H2B	-8.3191	2.1870	±1.5430	1.1700	0.978 04
O1	-0.4137	1.2962	0.0000	1.8400	0.744 47	H3A	-2.1280	-3.1132	0.0000	1.1700	0.978 04
O2	0.4137	-1.2962	0.0000	1.8400	0.744 47	H3B	-4.8006	-3.1132	±1.5430	1.1700	0.978 04
N1	-3.9097	5.0757	0.0000	1.7000	0.751 97	H4A	5.6914	-5.7056	0.0000	1.1700	0.978 04
N2	-7.6892	1.2962	0.0000	1.7000	0.751 97	H4B	3.0189	-5.7056	±1.5430	1.1700	0.978 04
N3	-3.9097	-2.4833	0.0000	1.7000	0.751 97	H5A	8.3191	0.4855	0.0000	1.1700	0.978 04
N4	3.9097	-5.0757	0.0000	1.7000	0.751 97	H5B	8.3191	-2.1870	±1.5430	1.1700	0.978 04
N5	7.6892	-1.2962	0.0000	1.7000	0.751 97	H6A	2.1280	3.1132	0.0000	1.1700	0.978 04
N6	3.9097	2.4833	0.0000	1.7000	0.751 97	H6B	4.8006	3.1132	±1.5430	1.1700	0.978 04
H1A	-5.6914	5.7056	0.0000	1.1700	0.978 04						
				C. $[(NH_3)_2Cu(O_2,OH)Cu(NH_3)_2]^{1+}$ (3)							
outer sphere	0.0000	1.1667	0.0000	9.0644	0.766 96	N4	5.0972	-3.3390	0.0000	1.7000	0.751 97
Cu1	-3.4016	0.0388	0.0000	2.9500	0.706 97	H1A	-6.5430	3.6094	0.0000	1.1700	0.978 04
Cu2	3.4016	0.0388	0.0000	2.9500	0.706 97	H1B	-7.7420	1.2209	±1.5430	1.1700	0.978 04
O1	-1.3606	2.9929	0.0000	1.8400	0.744 47	H2A	-3.7874	-4.7012	0.0000	1.1700	0.978 04
O2	1.3606	2.9929	0.0000	1.8400	0.744 47	H2B	-6.1759	-3.5023	±1.5430	1.1700	0.978 04
O-H	0.0000	-1.6086	0.0000	1.8400	0.744 47	H3A	6.5430	3.6094	0.0000	1.1700	0.978 04
H-O	0.0000	-3.4984	0.0000	1.1700	0.978 04	H3B	7.7420	1.2209	±1.5430	1.1700	0.978 04
N1	-6.7794	1.7345	0.0000	1.7000	0.751 97	H4A	3.7874	-4.7012	0.0000	1.1700	0.978 04
N2	-5.0972	-3.3390	0.0000	1.7000	0.751 97	H4B	6.1759	-3.5023	±1.5430	1.1700	0.978 04
N3	6.7794	1.7345	0.0000	1.7000	0.751 97						
				D. $(NH_3)_2CuO_2$ (4)							
outer sphere	0.0000	0.0000	0.0000	5.9205	0.763 11	HNA	-1.7505	±4.4162	0.0000	1.1700	0.978 04
Cu	0.0000	0.0000	0.0000	2.9500	0.706 97	HNB	-3.6842	±2.5715	1.5430	1.1700	0.978 04
O	3.3637	±1.3341	0.0000	1.8400	0.744 47	HNC	-3.6842	±2.5715	-1.5430	1.1700	0.978 04
N	-2.6049	±2.7306	0.0000	1.7000	0.751 97						
				E. $[(NH_3)_2CuO_2Cu(NH_3)_2]^{2+}$ (5)							
outer sphere	0.0000	0.0000	0.0000	8.8294	0.765 98	H1A	-5.1142	±4.4162	0.0000	1.1700	0.978 04
Cu1	-3.3637 .	0.0000	0.0000	2.9500	0.706 97	H1B	-7.0479	±2.5715	1.5430	1.1700	0.978 04
Cu2	3.3637	0.0000	0.0000	2.9500	0.706 97	H1C	-7.0479	±2.5715	-1.5430	1.1700	0.978 04
O	0.0000	±1.3341	0.0000	1.8400	0.744 47	H2A	5.1142	±4.4162	0.0000	1.1700	0.978 04
N1	-5.9686	±2.7306	0.0000	1.7000	0.751 97	H2B	7.0479	±2.5715	1.5430	1.1700	0.978 04
N2	5.9686	±2.7306	0.0000	1.7000	0.751 97	H2C	7.0479	±2.5715	-1.5430	1.1700	0.978 04

[a] All distances are in bohrs (0.529177 bohr = 1 Å).

malism has also been applied to copper dimers with chloride and carbonate bridged structures.[22] In addition, we have recently applied the broken-symmetry $X\alpha$ formalism to the structurally defined trans bridged copper–peroxide complex $[(CuL)_2(O_2)]^{2+}$, for which we have obtained an extensive amount of spectral data.[23]

To understand the differences in electronic structure and bonding in copper–peroxide complexes, we have undertaken SCF-$X\alpha$-SW calculations on a series of copper–peroxide monomers and dimers with different peroxide binding geometries. This extends our earlier electronic structural studies on copper–peroxide systems[24] and provides a set a calculations with similar ligand environments that can be directly compared to provide insight into the electronic structural origin of the physical molecular properties. We use the results to describe and compare Cu–O and O–O bonding interactions, charge and spin distributions, and excited-

state transition energies, which are in turn compared to the experimental properties and reactivity of the metalloproteins and structural analogues.

Computational Methods

The standard version of the SCF-$X\alpha$-SW method was used to calculate the electronic structure of a series of five copper–peroxide complexes. The geometries of the end-on bound copper–peroxide monomer, $(NH_3)_3CuO_2$ (1), and the end-on trans μ-1,2 copper–peroxide dimer, $[(NH_3)_3CuO_2Cu(NH_3)_3]^{2+}$ (2), are based on the only structurally characterized end-on copper–peroxide complex, which has a Cu–O–O angle of 107.7° and Cu–O and O–O distances of 1.85 and 1.44 Å,[11] respectively. The structure of the end-on cis μ-1,2 copper–peroxide dimer, $[(NH_3)_2Cu(O_2,OH)Cu(NH_3)_2]^{1+}$ (3), is based on the related series of cobalt dimers,[25] idealized to a planar geometry with C_{2v} molecular symmetry and Cu–O and O–O bond lengths of 1.90 and 1.44 Å, respectively. The geometries of the side-on bound copper–peroxide monomer, $(NH_3)_2CuO_2$ (4), and dimer, $[(NH_3)_2CuO_2Cu(NH_3)_2]^{2+}$ (5), are based on the structurally characterized side-on dimer, which has Cu–O and O–O distances of 1.92 and 1.41 Å, respectively.[10a] All structures have been idealized to planar geometry with approximate square-planar coordination about each copper. The orientation of the calculated structures with respect to the molecular axes is shown in Figure 1. All atomic orbitals are defined with respect to this molecular coordinate system.

(21) (a) Cook, M.; Karplus, M. *J. Chem. Phys.* **1985**, *83*, 6344–6366. (b) Sontum, S. F.; Noodleman, L.; Case, D. A. In *The Challenge of d and f Electrons: Theory and Computation*; Salahub, D. R., Zerner, M. C., Eds.; ACS Symposium Series 394; American Chemical Society: Washington, DC, 1989; pp 366–377. (c) Noodleman, L.; Case, D. A.; Sontum, S. F. *J. Chim. Phys.* **1989**, *86*, 743–755.

(22) (a) Bencini, A.; Gatteschi, D. *J. Am. Chem. Soc.* **1986**, *108*, 5763. (b) Bencini, A. *J. Chim. Phys.* **1989**, *86*, 763–787.

(23) (a) Baldwin, M. J.; Ross, P. K.; Karlin, K. D.; Solomon, E. I. Unpublished results. (b) Ross, P. K. Ph.D. Thesis, Stanford University, 1990.

(24) Ross, P. K.; Solomon, E. I. *J. Am. Chem. Soc.* **1990**, *112*, 5871–5872.

(25) Neiderhoffer, E. C.; Timmons, J. H.; Martell, A. E. *Chem. Rev.* **1984**, *84*, 137–203.

Table II. Energy Levels and Charge Distributions for $(NH_3)_3CuO_2$ (1)

		energy,[b] eV	charge distribution, %							
	level		Cu	O1	O2	N1	N2	N3	int[a]	out[a]
$d_{x^2-y^2}$	17A'	−0.000	65	11	4	6	5	6	1	2
Π^*_v	7A''	−1.099	14	35	34	0	0	0	16	1
Π^*_σ	16A'	−1.861	16	13	54	3	3	0	9	2
	15A'	−2.626	95	1	2	0	0	0	1	0
	6A''	−2.781	93	0	4	0	0	0	2	0
	14A'	−2.784	90	0	3	0	1	0	6	0
	5A''	−2.829	85	0	11	0	0	0	3	0

[a] int represents the intersphere region, and out represents the outer-sphere region. [b] Energies have been scaled as in Figure 2.
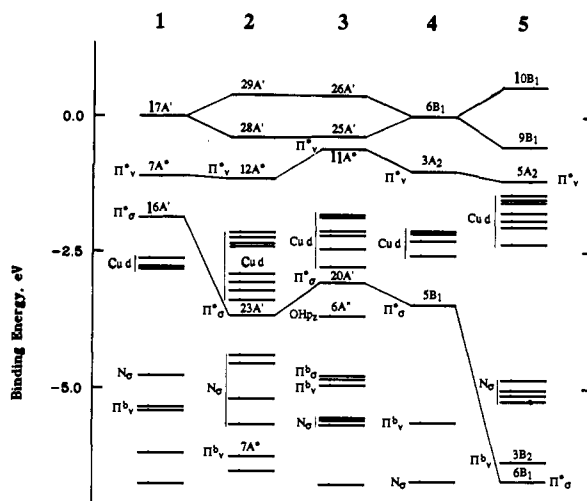

Figure 2. Energy level diagrams of 1–5 with copper sphere radii of 2.95 bohr. The energy scale has been linearly shifted such that 0 eV is centered between the HOMO and LUMO of the dimers and equal to the half-occupied level of the monomers.

Spin-restricted SCF-Xα-SW calculations were performed on the monomer structures 1 and 4, and according to the procedure of Noodleman,[17] spin-unrestricted broken-symmetry SCF-Xα-SW calculations were performed on the dimer structures 2, 3, and 5. Input parameters for the calculations including the position of the atoms, sphere radii, and α values are given in Table I. The calculations were considered to be converged when the largest relative change in the potential between subsequent iterations was less than 1×10^{-3} with a virial ratio, $-2T/V$, of 1.000 ± 0.001. The α values used in the atomic regions were those determined by Schwarz,[26] and those in the inter- and outer-sphere regions were weighted averages of the atomic α values based on the number of valence electrons in the neutral free atoms. All calculations were performed with copper, oxygen, nitrogen, and hydrogen sphere radii fixed at 2.95, 1.84, 1.70, and 1.17 bohr, respectively. These are averaged values of sphere radii based on the Norman criteria,[27] except for the copper sphere radii which were increased to correct for the tendency of the Norman criteria to overestimate the covalency of the metal ion.[28] Calculations were also performed on all structures with atomic sphere radii determined by the Norman criteria and with the copper sphere radii fixed at 2.60 Å. One-electron energies and charge distributions from all calculations are presented in the supplementary material.

Results and Analysis

A. Copper–Peroxide Bonding. 1. End-On Monomer.
The end-on monomer, $(NH_3)_3CuO_2$ (1), has a square-planar coordination environment with a peroxide anion bound end-on to a cupric ion and C_s total molecular symmetry. Energies and charge distributions of the two-electron energy levels from spin-restricted SCF-Xα-SW calculations on 1 with a copper sphere radius of 2.95
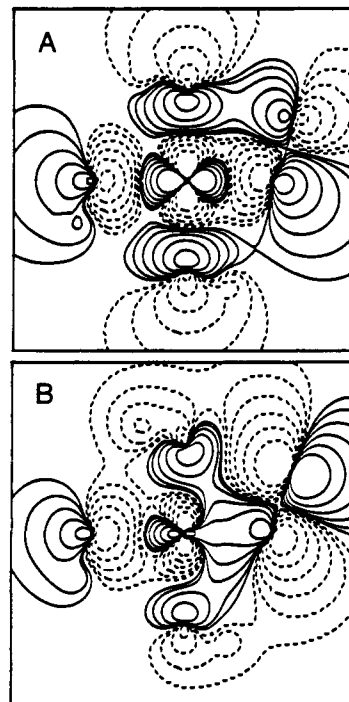
(26) (a) Schwarz, K. *Phys. Rev. B* **1972**, *5*, 2466–2468. (b) Schwarz, K. *Theor. Chim. Acta* **1974**, *34*, 225–231.

(27) (a) Norman, J. G., Jr. *J. Chem. Phys.* **1974**, *61*, 4630–4635. (b) Norman, J. G., Jr. *Mol. Phys.* **1976**, *31*, 1191–1198.

(28) (a) Gewirth, A. A.; Cohen, S. L.; Schugar, H. J.; Solomon, E. I. *Inorg. Chem.* **1987**, *26*, 1133–1146. (b) Didziulis, S. V.; Cohen, S. L.; Gewirth, A. A.; Solomon, E. I. *J. Am. Chem. Soc.* **1988**, *110*, 250–268. (c) Gewirth, A. A.; Solomon, E. I. *J. Am. Chem. Soc.* **1988**, *110*, 3811–3819.

Figure 3. Contour plots of the spin-restricted wave functions for the end-on monomer, 1, in the *xy* plane for (A) level 17A' (ground state) and (B) level 16A' (Π^*_σ). Contours are located at ±0.005, ±0.01, ±0.02, ±0.04, ±0.08, and ±0.16 $(e/bohr^3)^{1/2}$.

bohr are given in Table II. A diagram of these energy levels is presented in the first column of Figure 2. The ground state of this complex is the half-occupied Cu $d_{x^2-y^2}$, which is the highest occupied energy level (17A') in Table II. As shown in the contour plot of the wave function of level 17A' in Figure 3A, the Cu $d_{x^2-y^2}$ orbital is directed toward and delocalized onto the neighboring nitrogen and peroxide ligands and is antibonding with respect to the ligand orbitals. The next highest energy level (7A'') is primarily the peroxide Π^*_v orbital which is oriented vertical to the Cu–O–O plane. As shown in Table II, the peroxide Π^*_v only weakly interacts with the copper d orbitals, is mainly located on the peroxide, and is equally distributed over both oxygen atoms. In comparison, the level next highest in energy (16A') is primarily the in-plane peroxide Π^*_σ which has been stabilized due to a strong bonding interaction with the Cu $d_{x^2-y^2}$ orbital. The contour plot of the wave function of level 16A' in Figure 3B shows that the peroxide Π^*_σ orbital is oriented in the Cu–O–O plane has a bonding interaction with the Cu $d_{x^2-y^2}$, and the charge distribution in Table II indicates that level 16A' has more electron density on the terminal oxygen atom (O2) than on the oxygen atom bound to the copper (O1). This interaction between the ground-state Cu $d_{x^2-y^2}$ orbital (17A') and the peroxide Π^*_σ (16A') orbital is the primary contribution to the copper–peroxide bond. The Cu–O bonding interaction stabilizes the peroxide Π^*_σ below the Π^*_v (7A'') by 0.762 eV due to a strong σ bonding interaction. In addition, the Cu $d_{x^2-y^2}$ orbital (17A') is destabilized due to the reciprocal σ antibonding interaction (Figure 3A). The remaining filled d orbitals on the copper are the next highest energy levels and only interact with the ligands to a small extent. Calculations on 1 with Norman sphere radii and with a copper sphere radius increased to 2.60 bohr are qualitatively similar (supplementary material Table S1).

2. End-On Trans Dimer.
As shown in Figure 1, the end-on trans dimer, $[(NH_3)_3CuO_2Cu(NH_3)_3]^{2+}$ (2), has a square-planar coordination environment with an end-on peroxide bridging between the two cupric ions in a trans μ-1,2 geometry and C_{2h} total molecular symmetry. The one-electron energy level diagram from spin-unrestricted, broken-symmetry SCF-Xα-SW calculations on 2 with a copper sphere radius of 2.95 bohr is presented in the second column of Figure 2. Due to the nature of the broken-symmetry state, where the full molecular symmetry of C_{2h} is

Table III. Energy Levels and Charge Distributions for [(NH$_3$)$_3$CuO$_2$Cu(NH$_3$)$_3$]$^{2+}$ (2)

| | level | energy,[b] eV | charge distribution, % | | | | | |
			Cu1	Cu2	O1	O2	N$_{123}$[a]	N$_{456}$[a]
	unoccupied							
d$_{x^2-y^2}$	29A'↑	0.387	1	69	1	7	0	19
	29A'↓	0.387	69	1	7	1	19	0
	occupied							
d$_{x^2-y^2}$	28A'↑	−0.387	66	2	7	0	22	0
	28A'↓	−0.387	2	66	0	7	0	22
Π*$_v$	12A''↑	−1.153	6	24	26	35	0	0
	12A''↓	−1.153	24	6	35	26	0	0
	27A'↑	−2.142	2	88	3	4	0	1
	27A'↓	−2.142	88	2	4	3	1	0
	26A'↑	−2.236	1	94	1	0	0	0
	26A'↓	−2.236	94	1	0	1	0	0
	11A''↑	−2.348	3	93	2	0	0	0
	11A''↓	−2.348	93	3	0	2	0	0
	10A''↑	−2.408	17	67	13	0	0	0
	10A''↓	−2.408	67	17	0	13	0	0
	25A'↑	−2.918	80	5	7	4	2	0
	25A'↓	−2.918	5	80	4	7	0	2
	24A'↑	−3.068	91	2	1	1	2	0
	24A'↓	−3.068	2	91	1	1	0	2
	9A''↑	−3.218	98	0	0	0	0	0
	9A''↓	−3.218	0	98	0	0	0	0
	8A''↑	−3.384	68	13	2	13	0	0
	8A''↓	−3.384	13	68	13	2	0	0
Π*$_σ$	23A'↑	−3.661	26	13	19	26	7	8
	23A'↓	−3.661	13	26	26	19	8	7

[a] N$_{123}$ and N$_{345}$ represent the sum of the contributions of all nitrogen atoms on the right and left sides of the molecule. [b] Energies have been scaled as in Figure 2.
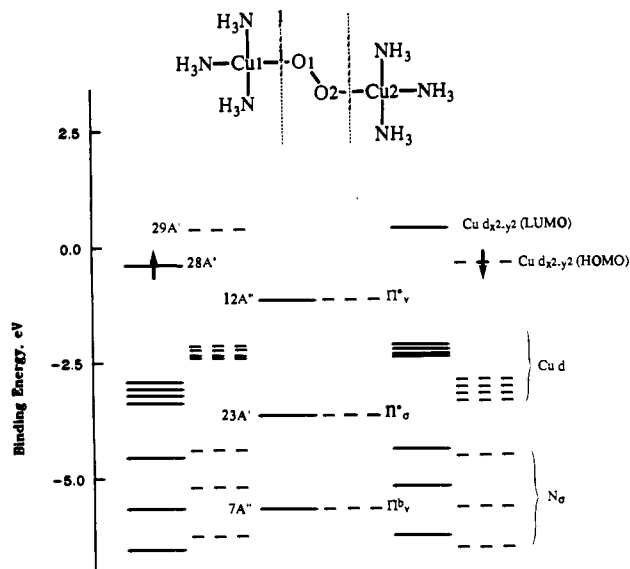
H$_3$N
H$_3$N—Cu1—O1   NH$_3$
H$_3$N   O2—Cu2—NH$_3$
                    NH$_3$

Figure 4. Expanded view of the energy level diagram of the end-on trans dimer, **2**. The spin-up (—) and spin-down (- - -) levels are grouped according to their distributions on the left, middle, and right sides of the molecule. The energies have been scaled as in Figure 2.

lowered to C_s and an equal but opposite up–down spin symmetry is imposed on opposite halves of the dimer, the energy levels are partially localized onto half of the molecule and each spin-up electron is energetically degenerate with a spin-down electron on the opposite side of the molecule. The spin-up and spin-down orbitals are images of one another under inversion for the end-on trans dimer. The extent of localization of the orbitals is given by the charge distributions presented in Table III and represented in Figure 4, which shows an expanded view of the energy level diagram where the spin-up and spin-down levels are grouped according to their distributions on the left, middle, and right sides of the molecule. Spin polarization in the broken-symmetry state causes a large splitting between the spin-up and spin-down d
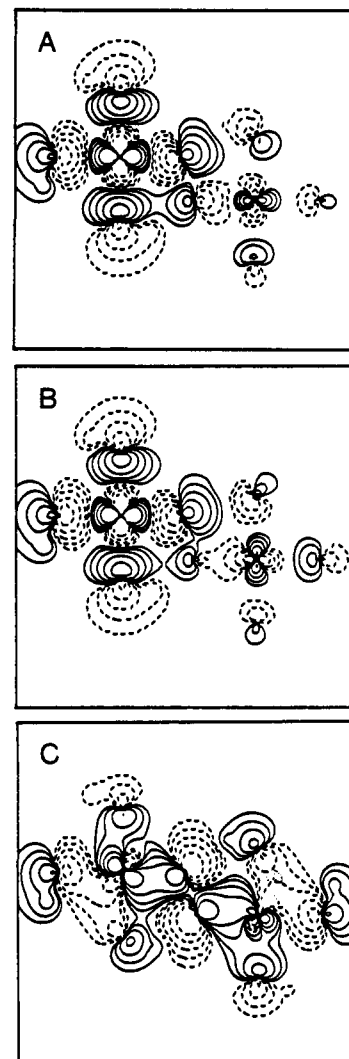

Figure 5. Contour plots of the partially localized, broken-symmetry wave functions for the end-on trans dimer, **2**, in the *xy* plane for (A) level 29A'↓ (LUMO), (B) level 28A'↑ (HOMO), and (C) level 23A'↑ (Π*$_σ$). Contours are located at ±0.01, ±0.02, ±0.04, ±0.08, and ±0.16 (e/bohr^3)$^{1/2}$.

orbitals on a given copper (e.g., the splitting of levels 28A'↑ and 29A'↓) as can be seen in Figure 4.

The ground state of **2** has two weakly coupled electrons in the half-occupied d$_{x^2-y^2}$ orbitals on each copper. As shown in Figure 5A, the lowest energy unoccupied level (29A'↓) is primarily the spin-down Cu d$_{x^2-y^2}$ orbital localized on Cu1 (left) and is partially delocalized into the (+)d$_{x^2-y^2}$ orbital on Cu2 (right). The highest energy occupied level (28A'↑), shown in Figure 5B, is primarily the corresponding spin-up Cu1 d$_{x^2-y^2}$ orbital and delocalized into the (−)d$_{x^2-y^2}$ orbital on Cu2. Levels 29A'↑ and 28A'↓ are the degenerate, inversion-symmetry images localized on Cu2. Both levels 29A' and 28A' have strong antibonding interactions with the nitrogen and peroxide ligands, which causes them to be higher in energy than the other filled Cu d orbitals. In addition, the positive linear combination[29] of Cu d$_{x^2-y^2}$ orbitals in level 29A'↓ (Figure 5A) has an antibonding interaction between the peroxide orbital and Cu2, which causes it to be higher in energy than the negative linear combination of Cu d$_{x^2-y^2}$ orbitals in level 28A'↑, which has a corresponding bonding interaction between the peroxide and Cu2 (Figure 5B).

As shown in the middle columns of Figure 4, the highest energy level primarily located on the oxygen atoms is 12A'', mainly

(29) All atomic orbitals are defined with respect to the molecular coordinate system indicated to the right of Figure 1. Therefore, a positive linear combination of d$_{x^2-y^2}$ orbitals on the two copper atoms of dimer **2** has the positive lobe of each orbital oriented along the molecular *x* axis.

Copper–Peroxide Complexes

J. Am. Chem. Soc., Vol. 113, No. 9, 1991 3251

Table IV. Energy Levels and Charge Distributions for
$[(NH_3)_2Cu(O_2,OH)Cu(NH_3)_2]^{1+}$ (3)

	level	energy,[b] eV	Cu1	Cu2	O1	O2	OH	N_{12}[a]	N_{34}[a]
	unoccupied								
d_{xy}	26A′↑	0.372	20	46	6	8	8	3	7
	26A′↓	0.372	46	20	8	6	8	7	3
	occupied								
d_{xy}	25A′↑	−0.372	50	27	3	1	2	10	5
	25A′↓	−0.372	27	50	1	3	2	5	10
Π^*_v	11A″↑	−0.604	8	12	33	35	0	0	0
	11A″↓	−0.604	12	8	35	33	0	0	0
	10A″↑	−1.816	17	55	0	0	22	0	0
	10A″↓	−1.816	55	17	0	0	22	0	0
	24A′↑	−1.867	10	67	6	12	0	2	2
	24A′↓	−1.867	67	10	12	6	0	2	2
	23A′↑	−2.113	8	86	2	0	0	0	0
	23A′↓	−2.113	86	8	0	2	0	0	0
	9A″↑	−2.130	27	61	8	1	0	0	0
	9A″↓	−2.130	61	27	1	8	0	0	0
	22A′↑	−2.205	58	28	8	1	0	2	1
	22A′↓	−2.205	28	58	1	8	0	1	2
	21A′↑	−2.443	94	1	0	0	0	1	0
	21A′↓	−2.443	1	94	0	0	0	0	1
	8A″↑	−2.452	63	32	0	0	3	0	0
	8A″↓	−2.452	32	63	0	0	3	0	0
	7A″↑	−2.784	60	24	3	9	0	0	0
	7A″↓	−2.784	24	60	9	3	0	0	0
Π^*_σ	20A′↑	−3.072	33	21	18	22	0	2	2
	20A′↓	−3.072	21	33	22	18	0	2	2

[a] N_{12} and N_{34} represent the sum of the contributions of all nitrogen atoms on the right and left sides of the molecule. [b] Energies have been scaled as in Figure 2.

composed of out-of-plane peroxide Π^*_v orbital which has a weak interaction with the Cu $d_{xz,yz}$ orbitals. Grouped together at deeper energy and also split by spin polarization are the filled Cu d orbitals which only weakly interact with the ligands. Also localized on the oxygen atoms, level 23A′, shown in Figure 5C, lies below the filled Cu d orbitals and is primarily composed of the in-plane peroxide Π^*_σ orbital which has been stabilized by a strong σ bonding interaction with the ground-state Cu $d_{x^2-y^2}$ orbitals. This bonding interaction between the Cu $_{x^2-y^2}$ and peroxide Π^*_σ is the dominant contribution to the copper–peroxide bond and stabilizes the Π^*_σ below the Π^*_v orbital (12A″), leading to a large Π^*_v–Π^*_σ splitting of 2.508 eV. Calculations on **2** with Norman sphere radii and with the copper sphere radii increased to 2.60 bohr are qualitatively similar (supplementary material Table S2). In addition, these results are in close agreement with calculations on an end-on trans dimer with trigonal-bipyramidal coordination which closely models the structurally characterized model, $[(CuL)_2(O_2)]^{2+}$.[23]

3. End-On Cis Dimer. The end-on cis dimer, $[(NH_3)_2Cu-(O_2,OH)Cu(NH_3)_2]^{1+}$ (3), has an approximate square-planar coordination with a bridging hydroxide anion and an end-on peroxide bridging between two copper(II) ions in a cis μ-1,2 geometry with C_{2v} total molecular symmetry. Energies and charge distributions of the one-electron energy levels from spin-unrestricted, broken-symmetry SCF-Xα-SW calculations on **3** with a copper sphere radius of 2.95 bohr are given in Table IV. The energy level diagram is presented in the third column of Figure 2 using the broken-symmetry C_s point group representations. Figure 6 shows an expanded view of the energy level diagram where the spin-up and spin-down levels are grouped according to their distributions on the left, middle, and right sides of the molecule. As shown in Table IV, the extent of localization of **3** due to the broken-symmetry procedure is not complete, with level 25A′↑ having 50% of the electron density on Cu1 and 27% on Cu2.

The broken-symmetry ground state of **3** has two weakly coupled electrons in the half-occupied d_{xy} orbitals which are partially localized on each copper. As shown in Figure 7A, the lowest energy unoccupied level (LUMO), 26A′↓, is a positive linear combination of spin-down Cu d_{xy} orbitals, localized mainly on Cu1
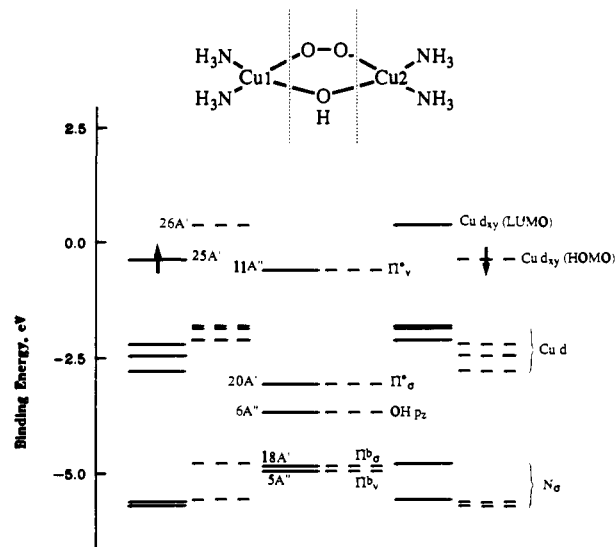

Figure 6. Expanded view of the energy level diagram of the end-on cis dimer, **3**. The spin-up (—) and spin-down (- - -) levels are grouped according to their distributions on the left, middle, and right sides of the molecule. The energies have been scaled as in Figure 2.
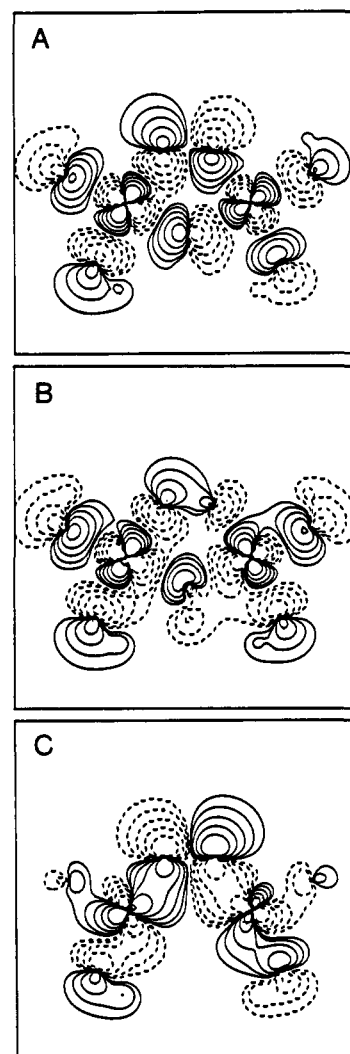

Figure 7. Contour plots of the broken-symmetry wave functions for the end-on cis dimer, **3**, in the xy plane for (A) level 26A′↑ (LUMO), (B) level 25A′↓ (HOMO), and (C) level 23A′↑ (Π^*_σ). Contours are located at ±0.01, ±0.02, ±0.04, ±0.08, and ±0.16 (e/bohr³)$^{1/2}$.

and delocalized into the (+)d_{xy} orbital on Cu2. The corresponding highest energy occupied level (HOMO), 25A′↑, is primarily the

Table V. Energy Levels and Charge Distributions for $(NH_3)_2CuO_2$ (4)

level		energy,[b] eV	Cu	O[a]	N[a]	H[a]	int[a]	out[a]
d_{xy}	$6B_1$	0.000	60	30	7	0	0	2
Π^*_v	$3A_2$	−1.017	11	77	0	0	11	1
	$8A_1$	−2.109	94	3	0	0	2	0
	$3B_2$	−2.152	92	6	0	0	2	0
	$7A_1$	−2.305	96	0	1	0	3	0
	$2A_2$	−2.572	90	7	0	0	3	0
Π^*_σ	$5B_1$	−3.473	42	52	4	0	0	2

charge distribution, %

[a] O, N, and H represent the sum of the contributions of all equivalent atoms. int and out represent the intersphere and outersphere regions. [b] Energies have been scaled as in Figure 2.

spin-up Cu1 d_{xy} orbital and is delocalized into the Cu2 (−)d_{xy} orbital, forming a negative linear combination of Cu d_{xy} orbitals as shown in Figure 7B. Levels 26A′↑ and 25A′↓ are the degenerate, mirror-symmetry images mainly centered on Cu2. As shown in Figure 6 and Table IV, the next highest energy level, 11A″, is centered on the peroxide and mainly composed of the out-of-plane peroxide Π^*_v orbital weakly mixed with the Cu $d_{xz,yz}$ orbitals. The filled Cu d orbitals, grouped together to deeper energy, are followed by level 20A′ centered on the peroxide and level 6A″ centered on the hydroxide. Level 20A′, shown in Figure 7C, is primarily the in-plane peroxide Π^*_σ orbital which has been stabilized by a strong σ bonding interaction with the positive linear combination of Cu d_{xy} orbitals which form the LUMO (26A′). This bonding interaction between the Cu d_{xy} and peroxide Π^*_σ is the dominant contribution to the copper–peroxide bond and stabilizes the Π^*_σ below the Π^*_v orbital (11A″) by 2.468 eV and destabilizes the Cu d_{xy} LUMO (26A′) with respect to the HOMO (25A′). As exhibited in Figure 7A, the bridging hydroxide p_x orbital also interacts with the Cu d_{xy}, providing an additional destabilizing interaction on the LUMO (26A′). Calculations on 3 with Norman sphere radii and with the copper sphere radii increased to 2.60 bohr are qualitatively similar (supplementary material Table S3).

4. Side-On Monomer. The side-on monomer, $(NH_3)_2CuO_2$ (4), has an approximate square-planar coordination with a peroxide anion bound in a side-on η^2 manner to a single cupric ion with C_{2v} total molecular symmetry. The contour plot in Figure 8A of the total electron density from spin-restricted SCF-Xα-SW calculations on 4 with a copper sphere radius of 2.95 bohr shows that significant electron density lies along the Cu–O vectors, indicating that the peroxide occupies two unique coordination sites on the copper. This is consistent with the formal description of peroxide bound to the copper by two σ bonds directed along each Cu–O vector, rather than by a single π bond to the center of the peroxide. Energies and charge distributions of the two-electron energy levels are given in Table V. The energy level diagram is presented in the fourth column of Figure 2. The ground state of 4 is the half-occupied Cu d_{xy}, which is the highest occupied energy level ($6B_1$) in Table V. As shown in the contour plot of the wave function of level $6B_1$ in Figure 8B, the Cu d_{xy} orbital is directed toward and delocalized onto the neighboring nitrogen and peroxide ligands and is antibonding with respect to the ligand orbitals. The next highest energy level ($3A_2$) is primarily the peroxide Π^*_v orbital which is oriented vertical to the Cu–O–O plane. As shown in Table V, the peroxide Π^*_v only weakly interacts with the copper d orbitals (11% Cu character) and is mainly located on the peroxide. The filled d orbitals on the copper are the next highest energy levels in Figure 2 (column 4) and only interact with the ligands to a small extent. In comparison, the level next highest in energy ($5B_1$) is primarily the in-plane peroxide Π^*_σ which has been stabilized due to a strong bonding interaction with the Cu d_{xy} orbital. The contour plot of the wave function of level $5B_1$ in Figure 8C shows that the peroxide Π^*_σ orbital, oriented in the Cu–O–O plane, forms two σ bonds with the Cu d_{xy} orbital. These σ bonding interactions between the ground-state Cu d_{xy} orbital ($6B_1$) and the peroxide Π^*_σ ($5B_1$) orbital are the primary contributions to the two copper–peroxide bonds in Figure
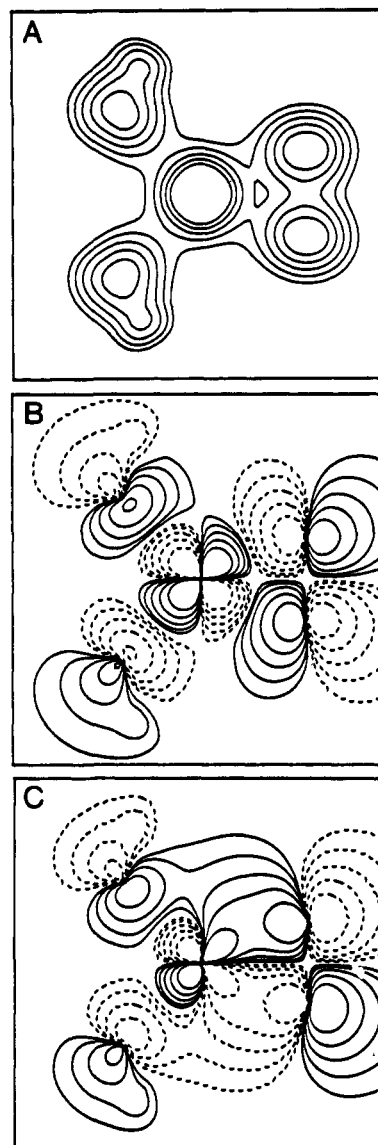

Figure 8. Contour plots for the side-on monomer, 4, in the xy plane for (A) the total electron density, (B) the spin-restricted wave function of level $6B_1$ (ground state), and (C) the wave function of level $5B_1$ (Π^*_σ). Contours for (A) are located at 0.06, 0.12, 0.24, 0.48, 0.96, $e/bohr^3$. Contours for (B) and (C) are located at ±0.01, ±0.02, ±0.04, ±0.08, and ±0.16 $(e/bohr^3)^{1/2}$.

8A. The Cu–O bonding interactions stabilize the peroxide Π^*_σ level below the Π^*_v ($3A_2$) by 2.456 eV, while destabilizing the Cu d_{xy} with respect to the other filled Cu d orbitals. Calculations on 4 with Norman sphere radii and with a copper sphere radius increased to 2.60 bohr are qualitatively similar (supplementary material Table S4).

5. Side-On Dimer. The side-on dimer, $[(NH_3)_2CuO_2Cu(NH_3)_2]^{2+}$ (5), has an approximate square-planar coordination environment with a peroxide anion bridging between two copper ions in a side-on μ-η^2:η^2 geometry with D_{2h} molecular symmetry. The contour plot in Figure 9A of the total electron density from spin-unrestricted, broken-symmetry SCF-Xα-SW calculations on 5 shows that significant electron density lies along the Cu–O vectors, indicating that the peroxide occupies two coordination sites on each copper and forms a total of four Cu–O σ bonds. The one-electron energy level diagram from calculations on 5 with a copper sphere radius of 2.95 bohr is presented in the fifth column of Figure 2 using the broken-symmetry designations of the C_{2v} point group. Figure 10 shows an expanded view of the energy level diagram where the spin-up and spin-down levels are grouped according to their distributions on the left, middle, and right sides of the molecule. As shown by the charge distributions in Table
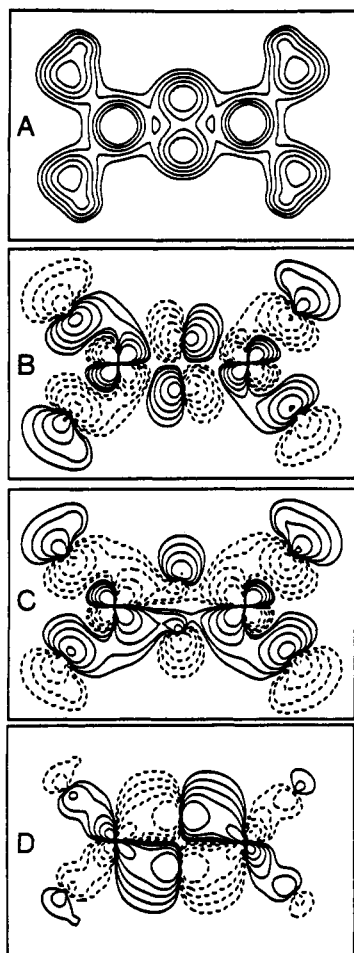
Copper-Peroxide Complexes

J. Am. Chem. Soc., Vol. 113, No. 9, 1991 3253

Figure 9. Contour plots for the side-on dimer, **5**, in the xy plane for (A) the total electron density, (B) the broken-symmetry wave function of level $10B_1$ (LUMO), (C) the wave function of level $9B_1$ (HOMO), and (D) the wave function of level $6B_1$ (Π^*_σ). Contours for (A) are located at 0.06, 0.12, 0.24, 0.48, 0.96 e/bohr^3. Contours for (B)–(D) are located at ±0.01, ±0.02, ±0.04, ±0.08, and ±0.16 (e/bohr^3)$^{1/2}$.

VI, the ground-state wave function of **5** exhibits significant delocalization over both copper centers, with the HOMO level $9B_1\uparrow$ having 46% of the electron density on Cu1 and 29% on Cu2.

As shown in Figure 9B, the lowest energy unoccupied level (LUMO), $10B_1\downarrow$, is a positive linear combination of spin-down Cu d_{xy} orbitals, with the most electron density centered on Cu1 but significantly delocalized into the $(+)d_{xy}$ orbital on Cu2. The corresponding highest energy occupied level (HOMO), $9B_1\uparrow$, is primarily the spin-up Cu1 d_{xy} orbital and is delocalized into the Cu2 $(-)d_{xy}$ orbital, forming a negative linear combination of Cu d_{xy} orbitals as shown in Figure 9C. Levels $10B_1\uparrow$ and $9B_1\downarrow$ are the degenerate, mirror-symmetry images mainly centered on Cu2. As shown in Figure 10 and Table VI, the next highest energy level, $5A_2$, is centered on the peroxide and mainly composed of the out-of-plane peroxide Π^*_v orbital weakly mixed with the Cu $d_{xz,yz}$ orbitals. The filled Cu d orbitals, grouped together to deeper energy, are followed by the copper–nitrogen σ bonding levels and levels $3B_2$ and $6B_1$ both centered on the peroxide. Level $3B_2$ is the out-of-plane Π^b_v orbital on the peroxide, and level $6B_1$, shown in Figure 9D, is primarily the in-plane peroxide Π^*_σ orbital.

The major contribution to the strength of the four copper–peroxide bonds is the σ bonding interaction between the positive linear combination of the Cu d_{xy} orbitals (LUMO) and the in-plane peroxide Π^*_σ orbital. The Π^*_σ orbital undergoes significant stabilization due to the bonding interaction with the Cu d_{xy}, resulting in a Π^*_v–Π^*_σ splitting of 5.528 eV and the $6B_1$ (Π^*_σ) level in Figure 9D lying below the N_σ levels and even below the peroxide Π^b_v level ($3B_2$). In addition, the reciprocal σ antibonding interaction between the positive combination of Cu d_{xy} orbitals and the Π^*_σ (Figure 9B) destabilizes the LUMO ($10B_1$) with
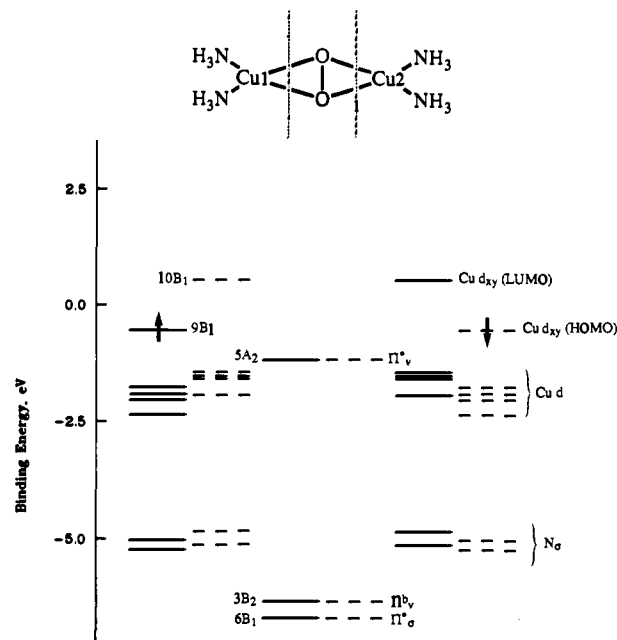

Figure 10. Expanded view of the energy level diagram of **5**. The spin-up (—) and spin-down (- - -) levels are grouped according to their distributions on the left and right sides of the molecule. The energies have been scaled as in Figure 2.

Table VI. Energy Levels and Charge Distributions for $[(NH_3)_2CuO_2Cu(NH_3)_2]^{2+}$ (**5**)

| | level | energy,[b] eV | charge distribution, % | | | | | | |
			Cu1	Cu2	O[a]	N1[a]	N2[a]	int[a]	out[a]
d_{xy}	unoccupied								
	$10B_1\uparrow$	0.545	27	44	12	6	9	0	0
	$10B_1\downarrow$	0.545	44	27	12	9	6	0	0
d_{xy}	occupied								
	$9B_1\uparrow$	−0.545	46	29	4	12	7	0	0
	$9B_1\downarrow$	−0.545	29	46	4	7	12	0	0
Π^*_v	$5A_2\uparrow$	−1.177	12	27	57	0	0	4	0
	$5A_2\downarrow$	−1.177	27	12	57	0	0	4	0
	$13A_1\uparrow$	−1.430	4	92	1	0	1	1	0
	$13A_1\downarrow$	−1.430	92	4	1	1	0	1	0
	$5B_2\uparrow$	−1.519	17	76	5	0	0	1	0
	$5B_2\downarrow$	−1.519	76	17	5	0	0	1	0
	$12A_1\uparrow$	−1.578	1	95	1	0	2	1	0
	$12A_1\downarrow$	−1.578	95	1	1	2	0	1	0
	$11A_1\uparrow$	−1.762	92	4	1	2	0	1	0
	$11A_1\downarrow$	−1.762	4	92	1	0	2	1	0
	$10A_1\uparrow$	−1.903	95	1	1	2	0	0	0
	$10A_1\downarrow$	−1.903	1	95	1	0	2	0	0
	$4A_2\uparrow$	−1.922	29	62	7	0	0	1	0
	$4A_2\downarrow$	−1.922	62	29	7	0	0	1	0
	$4B_2\uparrow$	−2.031	79	20	1	0	0	0	0
	$4B_2\downarrow$	−2.031	20	79	1	0	0	0	0
	$3A_2\uparrow$	−2.357	60	12	25	0	0	3	0
	$3A_2\downarrow$	−2.357	12	60	25	0	0	3	0
Π^*_σ	$6B_1\uparrow$	−6.705	22	21	56	0	0	0	0
	$6B_1\downarrow$	−6.705	21	22	56	0	0	0	0

[a] O, N1, and N2 represent the sum of the contributions of all equivalent atoms. int and out represent the intersphere and outersphere regions. [b] Energies have been scaled as in Figure 2.

respect to the HOMO ($9B_1$). A second important contribution to copper–peroxide bonding can be seen in Figure 9C, which shows the negative combination of Cu d_{xy} orbitals ($9B_1$, HOMO) forming a bonding interaction with the peroxide σ^* orbital. The peroxide σ^* orbital, which is unoccupied and lies to higher energy, acts to stabilize the HOMO with respect to the LUMO. To our knowledge, this is the first observation of the peroxide σ^* acting as a π acceptor orbital. The Π^*_σ donor and σ^* acceptor interactions combine to increase the HOMO–LUMO splitting and lead to significantly stable copper–peroxide structure. Calculations

3254 *J. Am. Chem. Soc., Vol. 113, No. 9, 1991*

Ross and Solomon

Table VII. Total Effective Electron Charge on Oxygen Atoms

	$Q(i)$	$QF(i)$	$Q_{eff}(i)$
end-on mono, **1** (O1)	7.70	8.10	8.25
1 (O2)	7.85	8.31	8.33
trans dimer, **2**	7.68	7.85	7.85
cis dimer, **3**	7.65	7.88	8.05
side-on mono, **4**	7.68	7.93	8.22
side-on dimer, **5**	7.46	7.50	7.45

Table VIII. Ground-State Singlet–Triplet Splitting, $-2J^a$

	trans dimer, $\mathbf{2}^b$	cis dimer, $\mathbf{3}^c$	side-on dimer, $\mathbf{5}^c$
Cu = 2.95 bohr	100	3040	5675
Cu = 2.60 bohr	1150	5950	11400
Cu ≈ 2.39 bohr^d	2300	9250	11800

^{a}All energies are given in cm^{-1}. ^{b}Weak coupling limit (eq 1). ^{c}Strong coupling limit (eq 2). ^{d}Norman sphere radii.

on **5** with Norman sphere radii and with copper sphere radii increased to 2.60 bohr are qualitatively similar (supplementary material Table S5). However, the degree of stabilization of the Π^*_σ level varies with the size of the copper sphere radius, due to the large overlap of the copper and oxygen atomic spheres in this structure.

B. O–O Bonding. One property of the calculations of particular importance is the strength of the peroxide bond which directly relates to the O–O force constant and, thus, the O–O stretching frequency. Both oxyhemocyanin[6] and the structurally characterized side-on dimer, [Cu(HB(3,5-iPr$_2$pz)$_3$]$_2$(O$_2$),[10] have low O–O stretching frequencies of 750 and 741 cm^{-1}, while the structurally characterized end-on trans dimer, [(CuL)$_2$(O$_2$)]$^{2+}$,[23] and the end-on monomer analogue, [Cu$_2$(XYL–O–)O$_2$]$^{1+}$,[15] have larger values for ν_{O-O} of 832 and 803 cm^{-1}, respectively. Attempts have been made to estimate the O–O bond order on the basis of the electron charge density located on the oxygen atoms. We present three methods for calculating the charge on the oxygen atoms and apply them to the five copper–peroxide structures.

The most common method for determining the total electron charge on a given atom in the Xα-SW method is to simply integrate the charge contained in the atomic sphere.[30] Values of the total charge on a given oxygen atom, $Q(i)$, for the five different calculated structures are given in the first column of Table VII. However, this method does not include charge located in the interatomic and extramolecular regions. Cook and Karplus have devised a method for repartitioning the charge in these regions between the atomic spheres.[31] The values of the charge on a given oxygen atom after the extraatomic charge has been repartitioned, $QF(i)$, are given in the second column of Table VII. Case and Karplus have developed an alternative method of determining the effective charge on an atom on the basis of the value of the self-consistent potential near the nucleus of the atom.[32] The effective charge on an oxygen atom, Q_{eff}, is approximated by linear interpolation of the molecular potential between the potential of an oxygen atom and an oxygen anion and is given in the third column of Table VII.

For the end-on monomer, **1**, which has two symmetry inequivalent oxygen atoms, all three methods give the oxygen atom bound to the copper (O1) less electron density than the terminally bound oxygen atom (O2). This is a demonstration of the covalent, electron-donating nature of the O1 atom bound to the copper, consistent with the contour plot of the Π^*_σ level shown in Figure 3B. For structures **2** and **3**, with peroxide bridging end-on between two coppers, the first two methods, based on the charge in the atomic sphere, give quite similar values, while more variation in the charge on the oxygen atoms is evident in the last method. The greater amount of electron density on the peroxide in **3**, relative to **2**, is due to the bridging hydroxide, which donates electron density to the copper and diminishes the extent of donation from the peroxide. All three methods calculate values for the side-on monomer, **4**, which are intermediate between those of the end-on dimers, **2** and **3**, and the end-on monomer, **1**, while the side-on dimer, **5**, consistently has the smallest calculated electron density on the peroxide. Although the values for the effective charge on an atom given by the three methods are not quantitatively reliable,

trends in the values over the series of structures give insight into the electronic structure of these systems. From the calculations it is clear that the side-on dimer, **5**, has the least reduced form of bound dioxygen. This is consistent with the four σ donor interactions that the peroxide makes with the two coppers (Figure 9D). In contrast, the end-on monomer, **1**, which has only one σ bonding interaction with the copper (Figure 3B), has the most reduced peroxide. On the basis of this trend, it can be seen that the amount of charge on the peroxide is directly related to the ability of the peroxide to donate charge onto the copper and, hence, to the number and strength of σ donor bonding interactions. Furthermore, an estimation of the O–O bond strength and stretching frequency based on the charge on the peroxide follows the same trend with the end-on monomer, **1**, predicted to have the weakest O–O bond, the side-on monomer, **4**, to be slightly stronger, the end-on dimers, **2** and **3**, to be stronger still, and the side-on dimer, **5**, to have the strongest O–O bond. This trend in predicted O–O bond strengths is consistent with the observed O–O stretching frequencies for the end-on monomer analogue, [Cu$_2$-(XYL–O–)O$_2$]$^{1+}$, and the end-on trans dimer, [(CuL)$_2$(O$_2$)]$^{2+}$, of 803 and 832 cm^{-1}, respectively. However, it is inconsistent with the side-on dimer, **5**, having the strongest predicted O–O bond strength, since the analogous model complex, [Cu(HB(3,5-iPr$_2$pz)$_3$]$_2$(O$_2$), has an O–O stretching frequency of 741 cm^{-1}, which is one of the lowest observed O–O stretching frequencies for a copper–peroxide complex. Clearly, in addition to the total charge on the oxygen atoms, the specific orbital occupancy of electron density also plays an important role (vide infra).

C. Magnetic Interactions. The broken-symmetry formalism was specifically developed to treat the interactions between antiferromagnetically coupled transition-metal ions, and one of the advantages of this formalism is the ability to use projection operator techniques to determine the sign and magnitude of the ground-state superexchange interactions. The broken-symmetry ground state, represented by a single Slater determinant, is not a pure spin state but is rather a mixture of the singlet and triplet spin states. It has been demonstrated that in the limit of weakly interacting copper dimers, where the magnetic orbitals are localized on each metal, the energy of the broken-symmetry state is the average of the singlet- and triplet-state energies, and the ground-state singlet–triplet splitting, $-2J$ (H = $-2JS_1 \cdot S_2$), is twice the energy difference of the triplet and broken-symmetry states (eq 1).[17b]

$$-2J = 2[E_{S=1} - E_B] \qquad (1)$$

For more strongly interacting dimers, where the magnetic orbitals are delocalized over both coppers, the ground-state singlet–triplet splitting, $-2J$, is equal to the difference in energy of the triplet and broken-symmetry states (eq 2).[17,22b]

$$-2J = E_{S=1} - E_B \qquad (2)$$

For copper dimers, which have only two singly occupied magnetic orbitals, this energy difference can be directly calculated by the Slater transition-state method.[33] For example, the transition energy from the broken-symmetry state to the spin triplet ground state of the end-on trans dimer, **2** (Figure 4), can be calculated by moving half an electron from the 28A'↑ level to the 29A'↓ level. Since the ground-state wave function of **2** is highly localized (Figure 5A,B and Table III), the weak coupling limit

(30) Case, D. A.; Karplus, M. *J. Am. Chem. Soc.* **1977**, *99*, 6182–6194.
(31) (a) Cook, M.; Karplus, M. *J. Chem. Phys.* **1980**, *72*, 7–19. (b) Case, D. A.; Karplus, M. *Chem. Phys. Lett.* **1976**, *39*, 33–38.
(32) (a) Case, D. A.; Huynh, B. H.; Karplus, M. *J. Am. Chem. Soc.* **1977**, *99*, 6103–6105. (b) Case, D. A.; Huynh, B. H.; Karplus, M. *J. Am. Chem. Soc.* **1979**, *101*, 4433–4453.

(33) Slater, J. C. *The Self-Consistent Field for Molecules and Solids*; *Quantum Theory of Molecules and Solids*; McGraw-Hill: New York, 1974; Vol. 4.

(eq 1) is valid, resulting in a calculated value of 100 cm^{-1} for the ground-state singlet–triplet splitting. As presented in the first column of Table VIII, the calculated value of $-2J$ dramatically increases as the copper sphere radius is decreased. The experimentally observed value for the singlet–triplet splitting of 700 cm^{-1} [34] for the end-on trans dimer, $[(CuL)_2(O_2)]^{2+}$, falls within the range of values calculated by varying the radius of the copper sphere. These values represent moderately large antiferromagnetic superexchange interactions, which are solely transmitted through the peroxide bridge. The ground state of the end-on cis dimer, 3, can best be described as a dimer with intermediate coupling. As seen in Figure 7A,B and Table IV, the ground state is partially localized but to a smaller extent than the end-on trans dimer, 2. By use of the strong coupling limit of eq 2, large antiferromagnetic couplings ranging from 3040 to 9250 cm^{-1} were calculated for the ground-state superexchange interaction. The larger antiferromagnetic interaction and larger degree of delocalization of the end-on cis dimer, 3, relative to the end-on trans dimer, 2, derives from the additional contribution of the bridging hydroxide, as well as the peroxide, to the exchange coupling (see Figure 7A). The ground state of the side-on dimer, 5, is best described as a strongly coupled dimer. As seen in Figure 9B,C and Table VI, the ground-state wave function is significantly delocalized over both copper ions, and hence, eq 2 should be used to obtain a value for $-2J$. The ground state of 5 has the largest calculated antiferromagnetic coupling with values ranging from 5675 to 11 800 cm^{-1}. Although a lower limit of the singlet–triplet splitting has not been reported for the side-on dimer analogue, $[Cu(HB(3,5-iPr_2pz)_3]_2(O_2)$, the large antiferromagnetism calculated for 5 is consistent with its observed diamagnetism.

The magnitude of ground-state exchange interaction is dependent on two related effects: the amount of bridging ligand character in the ground-state wave function and the extent of delocalization of the wave function over the two metal sites. In the broken-symmetry formalism, the effects of electron exchange and correlation are directly related to the extent of overlap between the magnetic orbital wave functions and, hence, the extent of delocalization of the magnetic orbitals over the two metal centers. A greater delocalization and larger overlap of the wave functions result in a larger exchange interaction between the metals. The dependence of the calculated ground-state exchange interaction on the copper sphere radius is a direct result of the decreased covalency of the metal and greater localization of the spin orbital on each half of the dimer as the copper sphere size increases. As the copper sphere is increased, more charge is drawn into the copper sphere, making the molecule less covalent with less bridging ligand character mixed into the ground state. It is this bridging ligand character that provides the orbital superexchange pathway between the metals and provides a mechanism for the orbitals to delocalize between the two metal centers. The magnitude of the superexchange interaction is, therefore, related to the amount of peroxide character mixed into the ground state and the extent of delocalization between the two metal centers. For a given copper sphere radius the extent of delocalization for the three dimers gives the following trend in the magnitude of the exchange interaction: the end-on trans dimer, 2, is the least delocalized and has the smallest calculated exchange interaction, the end-on cis dimer, 3, has an intermediate delocalization and has a larger calculated ground-state exchange coupling, and the side-on dimer, 5, has the greatest delocalization and the largest calculated exchange interaction.

D. Excited-State Transition Energies. In the SCF-Xα-SW method excited-state transition energies can be calculated with the Slater transition-state method,[33] where half an electron from the donating orbital is transferred to an accepting orbital of the same spin (for spin-allowed transitions) or of opposite spin (for spin-forbidden transitions) and the difference in energy of these two states at convergence is equal to the transition energy. This method is more accurate than simply taking the difference in the one-electron energies of the ground state because it includes effects

(34) Karlin, K. D. Personal communication.

Table IX. Excited-State Transition Energies[a]

A. Calculated Transition-State Energies

	Π*$_v$	Π*$_\sigma$	lowest d–d	highest d–d
end-on monomer, 1	level 7A″	level 16A′	level 15A′	level 5A″
Cu = 2.30	12 600	16 900	31 100	38 600
Cu = 2.60	12 900	19 400	27 700	32 100
Cu = 2.95	13 500	19 800	22 900	24 600
end-on trans dimer, 2	level 12A″	level 23A′	level 27A′	level 8A″
Cu = 2.39	17 100	25 600	31 000	38 500
Cu = 2.60	16 400	29 900	26 600	32 200
Cu = 2.95	16 000	39 000	22 400	24 500
end-on cis dimer, 3	level 11A″	level 20A′	level 10A″	level 7A″
Cu = 2.37	10 600	19 500	26 800	35 000
Cu = 2.60	10 300	20 300	24 500	29 800
Cu = 2.95	10 600	29 200	19 600	22 200
side-on monomer, 4	level 3A$_2$	level 5B$_1$	level 8A$_1$	level 2A$_2$
Cu = 2.32	11 900	25 600	28 900	36 800
Cu = 2.60	12 200	27 600	26 100	31 600
Cu = 2.95	12 000	32 300	19 200	22 800
side-on dimer, 5	level 5A$_2$	level 6B$_1$	level 13A$_1$	level 3A$_2$
Cu = 2.40	17 800	33 700	27 700	37 100
Cu = 2.60	16 900	39 300[b]	24 700	30 600
Cu = 2.95	16 000	66 800	18 100	21 400

B. Experimental Charge-Transfer Transition Energies

	Π*$_v$	Π*$_\sigma$
end-on monomer,[c] $[Cu_2(XYL-O-)O_2]^{1+}$	16 000	19 900
end-on trans dimer,[d] $[(CuL)_2(O_2)]^{2+}$	16 500	19 120
side-on dimer,[e] $[Cu(HB(3,5-iPr_2pz)_3]_2(O_2)$	18 150	28 650

[a] All energies are given in cm^{-1}. [b] This Π*$_\sigma$ level is significantly mixed with an amine N$_\sigma$ level. [c] Reference 12. [d] Reference 11. [e] Reference 10.

of relaxation due to changes in the electron density distribution of the excited state. The excited-state transition energies for the Π*$_v$ and Π*$_\sigma$ charge-transfer transitions and lowest and highest energy ligand-field transitions calculated with different copper sphere radii are presented in Table IXA. The transition energies for the dimers 2, 3, and 5 have been calculated in the broken-symmetry formalism and represent transitions from the broken-symmetry ground state to an excited state of mixed-spin symmetry. As an example, the Π*$_v$ charge-transfer transition of the end-on trans dimer, 2, was calculated by moving half an electron from the 12A″↓ level, which is localized on the peroxide (middle of Figure 4 and Table III), to the 29A′↓ level, which is localized on Cu1. This represents a spin-allowed charge-transfer transition localized on the left side of the molecule.

The calculated excited-state transition energies presented in Table IXA exhibit a varied degree of dependence on the radius of the copper sphere. The Π*$_v$ charge-transfer transitions presented in the first column are relatively insensitive to the choice of sphere size. Conversely, the calculated energies of the Π*$_\sigma$ charge-transfer transitions shown in the second column of Table IXA exhibit a large dependence on the copper sphere size, increasing significantly as the copper radius is increased. In addition, the lowest and highest energy ligand-field transitions presented in the last two columns of Table IXA show a moderate dependence on the sphere size, decreasing by roughly 70% as the radius of the copper sphere is increased. The dependence of the calculated transition energies on the copper sphere radius is a direct result of changes in the extent of covalency of the metal atoms. As the copper sphere radius is increased, more charge is drawn into the sphere, destabilizing the metal d orbitals and stabilizing the ligand orbitals. The Π*$_\sigma$ excited state is affected to a much greater degree than other excited states because it has a larger overlap with the ground state and is the primary orbital responsible for electron donation to the metal.

Although the calculated ligand-field transitions decrease as the sphere size is increased, the calculated values are still higher in energy than the Π*$_v$ charge-transfer transitions and are generally
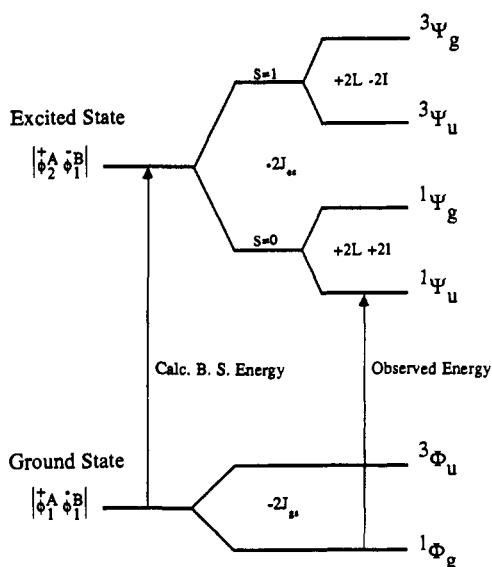
Figure 11. Energy level splitting diagram of the ground and excited states of a copper dimer. The ground state splits into a singlet and a triplet, and the excited state is split into four states: symmetric and antisymmetric combinations of singlets and triplets. The calculated transition energy is a difference in the average energy of the ground and excited states, while the observed transition is from the singlet ground state to the electric dipole allowed singlet excited state.

higher than those observed for known copper–peroxide complexes. This is most likely due to the planar geometry of the calculated structures compared to a more realistic square-pyramidal (C_{4v}) or trigonal-bipyramidal geometry. The calculated energies for the Π^*_v and Π^*_σ charge-transfer transitions of the end-on monomer, **1**, with a copper sphere radius of 2.95 bohr are in close agreement with the observed energies from the absorption spectrum of the end-on monomer analogue, $[Cu_2(XYL-O-)O_2]^{1+}$, which are presented in the first row of Table IXB. The calculated energies for the Π^*_v transitions in the trans dimer, **2**, and the side-on dimer, **5**, are also in good agreement with the observed transition energies of the related analogues. However, the calculated Π^*_σ charge-transfer energies for the dimers are significantly different from the experimental values. In calculations with the large sphere values of 2.95 bohr, the calculated Π^*_σ values are more than twice the observed values, and with the smallest radii, the values are still 5000–6000 cm^{-1} too large. Although the calculated Π^*_σ energies are not quantitatively accurate, they do follow the expected trend in the splitting between the Π^*_v and Π^*_σ orbitals, increasing from 0.8 eV in the end-on monomer to 2.5 eV for the end-on dimers and side-on monomer and further increasing to 5.5 eV for the side-on dimer.

In addition to the energy dependence of the calculated transition energies due to the copper sphere radius, the broken-symmetry formalism calculates transition energies that do not directly relate to the strongly coupled excited states which are experimentally observed in the absorption spectrum. Just as the ground state of a copper dimer is split into singlet and triplet components due to a ground-state exchange interaction, it is known that each excited state of a copper dimer is split into four components due to linear combinations of singlets and triplets.[35] The splittings between the ground- and excited-state components are shown on the right side of Figure 11. An excited-state exchange interaction splits the excited state into singlet and triplet components separated by $-2J_{es}$. The singlet and triplet components are further split into symmetric and antisymmetric (with respect to a given symmetry operation between the two coppers, e.g., inversion) components by Coulomb $(-2I)$ and exchange $(-2L)$ mediated excitation transfer interactions between the metal centers. The energy of the observed electric dipole allowed transition is the difference

from the $^1\Phi_g$ component of the ground state to the $^1\psi_u$ component of the excited state. However, because the broken-symmetry formalism is based on a single determinant, the calculated transition energy from the broken-symmetry ground state to the mixed-spin excited state corresponds to an average of the excited-state components as shown on the left side of Figure 11. Due to the large overlap of the Π^*_σ and Cu d_{xy} orbitals, the Π^*_σ charge-transfer excited state is expected to have a large antiferromagnetic exchange interaction, which contributes to an overestimation of the calculated transition energy. However, the Π^*_v excited-state splittings should be much smaller because the unpaired electrons occupy orthogonal orbitals which are much more localized toward opposite halves of the dimer. Therefore, the calculated transition energies for the Π^*_v excited state should compare more closely to observed values than the calculated energies for the Π^*_σ excited state. On the basis of a comparison of the calculated transition energies of the end-on trans and cis dimers and taking into account the systematic overestimation of the calculated transition Π^*_σ energies by a factor of 2 for the copper radius of 2.95 bohr, the absorption spectrum of the presently nonexistent cis dimer can reasonably be expected to have a low-lying Π^*_v transition near 10 500 cm^{-1} and an intense Π^*_σ transition near 14 600 cm^{-1}.

It should also be noted that when an intermediate copper sphere radius (2.60 bohr) is used, the Π^*_σ orbital in the side-on dimer, **5**, mixes significantly with the amine N_σ bonding levels, increasing the nitrogen orbital contribution to the Π^*_σ wave function in Figure 9D (see supplementary material Table S5B).[24] This type of amine N_σ mixing into the Π^*_σ excited state could be responsible for the observed enhancement of Cu–N vibrational modes in the resonance Raman spectrum of oxyhemocyanin. In addition, the extensive delocalization of the Π^*_σ level over both copper atoms of all three of the dimer calculations (see Tables III, IV, and VI) provides an explanation for lack of resonance enhancement of the Cu–O stretching modes in the resonance Raman spectrum of copper-peroxide dimers. In the copper–peroxide monomer, excitation from the Π^*_σ level shifts electron density from a Cu–O bonding level to an antibonding level, causing a distorting force which lengthens the Cu–O bond, leading to resonance enhancement of this vibrational mode. On going to a dimer, the charge-transfer excited state can be in either the strong or the weak coupling limit.[36] In the weak coupling limit, the charge-transfer excited state is predominantly localized on one part of the dimer, so that the excited-state distortion will simply reflect that of the monomer and thus result in resonance enhancement of the Cu–O vibrational mode. In the strong coupling limit, the excited state is delocalized over both copper atoms, which will lead to distorting forces on both metal centers that can cancel, resulting in little distortion of the Cu–O bonds. Thus, in the strong coupling limit the excited-state distortion of the dimer can be very different from that of the monomer. Insight into the extent of electronic coupling in the charge-transfer excited state of the dimer can be obtained from the excited-state wave function. In particular, the Π^*_σ levels in Tables III, IV, and VI show strong delocalization of this excited state onto both copper centers in the dimer. The difference in distortions for weakly and strongly coupled dimer excited states seems to provide an explanation for why the Cu–O stretching modes of oxyhemocyanin and the end-on trans dimer analogue, $[(CuL)_2(O_2)]^{2+}$, are not enhanced by excitation into the Π^*_σ excited state,[6,23] while enhancement of the Cu–O stretching mode has been observed by excitation from the Π^*_σ level of the end-on monomer analogue, $[Cu_2(XYL-O-)O_2]^{1+}$,[15] and by excitation from the weakly coupled Π^*_v level of the end-on trans dimer analogue, $[(CuL)_2(O_2)]^{2+}$.[23]

Discussion

One important goal of this study is to understand the nature of the copper–peroxide bond and how it is influenced by the geometry of the molecule and the changes that occur when the

(35) Ross, P. K.; Allendorf, M. D.; Solomon, E. I. *J. Am. Chem. Soc.* **1989**, *111*, 4009–4021.

(36) (a) McClure, D. S. *Can. J. Chem.* **1958**, *36*, 59–71. (b) Simpson, W. T.; Petterson, D. L. *J. Chem. Phys.* **1957**, *26*, 588–593.
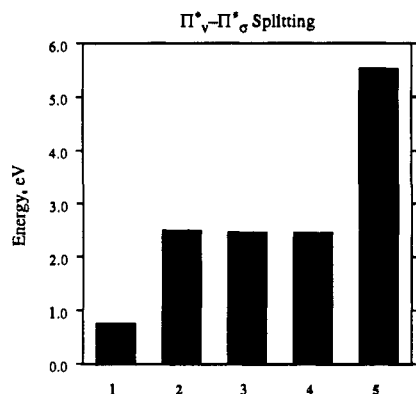
Copper-Peroxide Complexes

J. Am. Chem. Soc., Vol. 113, No. 9, 1991 3257

Figure 12. Energy difference between the peroxide Π^*_v and Π^*_σ levels for structures 1-5, calculated with copper sphere radii of 2.95 bohr.
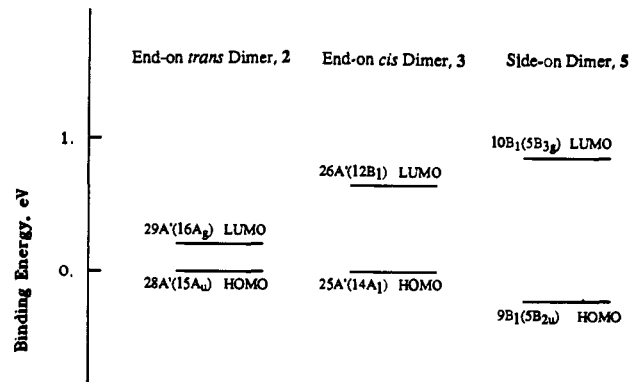

Figure 13. One-electron energy splittings between the HOMO and LUMO levels from the full symmetry SCF-Xα-SW calculations prior to breaking the symmetry of the dimers with copper sphere radii of 2.95 bohr. The energy levels are labeled with the broken-symmetry representations and the full symmetry representations in parentheses. The magnitude of the HOMO-LUMO splitting is proportional to the ground-state singlet-triplet splitting.

peroxide is bridged between two coppers. The series of five copper–peroxide structures that we have calculated provides an opportunity to compare the bonding in a set of monomers and dimers with different peroxide binding geometries but with similar ligand environments. Depending on the orientation of the ligands with respect to the molecular axes, these structures were found to have Cu d_{xy} or $d_{x^2-y^2}$ ground states due to destabilizing σ antibonding interactions with the ligands. In addition, the principal contribution to the copper–peroxide bond in all structures was found to be a strong σ bonding interaction between the Cu d_{xy} or $d_{x^2-y^2}$ ground state and the in-plane peroxide Π^*_σ orbital (see Figures 3A, 5A, 7A, 8B, and 9B). This interaction stabilizes the peroxide Π^*_σ orbital below the Π^*_v orbital which only weakly interacts with the copper d orbitals and remains at a fairly constant energy. Therefore, the splitting between the Π^*_v and Π^*_σ orbitals, presented in Figure 12, gives a rough measure of the strength of the copper–peroxide bonding interaction. Figure 12 demonstrates the dramatic effect that the peroxide bridging mode can have on the magnitude of the $\Pi^*_v-\Pi^*_\sigma$ splitting. The end-on monomer, 1, has only one Cu–O σ bonding interaction and consequently has the smallest $\Pi^*_v-\Pi^*_\sigma$ splitting. Structures 2-4, which each have two Cu–O σ bonds, all have approximately the same intermediate $\Pi^*_v-\Pi^*_\sigma$ splitting, while the side-on dimer, 5, has the largest $\Pi^*_v-\Pi^*_\sigma$ splitting due to the stabilizing effect of four Cu–O σ bonding interactions. It is important to note from Figure 9C that only in the case of the side-on dimer, 5, was an additional contribution to the copper–peroxide bond found where the peroxide σ^* orbital acts as a π acceptor stabilizing the Cu d_{xy} HOMO. This novel type of bonding interaction is found to influence significantly the electronic structure and physical properties of this side-on dimer complex.

Understanding how the peroxide O–O bond is influenced by changes in geometry is another important goal of this study. The end-on monomer, 1, has been found to have the most charge on the oxygen atoms and, therefore, has the most reduced peroxide. Furthermore, the side-on dimer, 5, which has the least amount of electron charge on the oxygen atoms, contains the least reduced peroxide unit. This trend in the charge on the peroxide is directly related to the ability of the peroxide to donate electron density onto the copper and, hence, is related to the strength and number of σ donor bonding interactions. It is these same bonding interactions that lead to the $\Pi^*_v-\Pi^*_\sigma$ splitting shown in Figure 12. The side-on dimer, 5, which contains the least reduced peroxide, has four σ Cu–O bonding interactions that donate a large amount of electron density to the copper and also lead to a large $\Pi^*_v-\Pi^*_\sigma$ splitting. The charge on the peroxide can also be related to the strength of the O–O bond and the O–O stretching frequency and predicts the correct trend for the end-on monomer and end-on trans dimer ν_{O-O} frequencies. In contrast, the side-on dimer, which has the lowest O–O stretching frequency, is not in agreement with the predicted trend based on the oxygen atom electron charge density. The unique bonding interaction between the π accepting peroxide σ^* orbital and the HOMO in the side-on dimer, 5, shifts a small amount of electron density from the σ donating Π^*_σ orbital

into the strongly antibonding (with respect to peroxide) σ^* level, resulting in a significant weakening of the peroxide bond and shifting of the O–O stretching frequency to lower energy. In addition to the total charge on the oxygen atoms, it is clear that the specific orbital occupation of the electron density also plays an important role in determining the observed O–O stretching frequency.

Broken-symmetry calculations on the three copper–peroxide dimers indicate that the ground-state exchange interactions follow a trend where the end-on trans dimer, 2, has the smallest calculated exchange coupling (which is still quite large, $-2J = 1150$ cm^{-1} for the intermediate sphere value of 2.60 bohr in Table VIII), the end-on cis dimer, 3, has an intermediate exchange coupling, and the side-on dimer, 5, has the largest calculated ground-state exchange interaction. Insight into the electronic structural origin of the magnitude of the exchange interaction can be obtained from the splitting between the HOMO and LUMO levels in the Xα calculations prior to breaking the symmetry, as $-2J$ is proportional to the splitting of the linear combinations of d_{xy} ($d_{x^2-y^2}$) orbitals on each Cu due to bonding interactions with the bridging ligands.[37] The HOMO–LUMO splitting for the end-on trans dimer, 2, which has a moderately large antiferromagnetic exchange interaction, is shown in the first column of Figure 13. The splitting is due solely to the destabilizing antibonding interaction of the peroxide Π^*_σ orbital with the 29A′ LUMO in broken symmetry or the 16A$_g$ LUMO in the full symmetry calculation prior to symmetry breaking. As shown in Figure 5A, the major orbital pathway for the exchange interaction through the peroxide in 2 involves the peroxide Π^*_σ orbital which couples the two coppers by mixing into the symmetric combination of Cu $d_{x^2-y^2}$ (LUMO) ground state. Like the end-on trans dimer, the peroxide provides a significant orbital pathway for the superexchange interaction in the end-on cis dimer, 3, through the Π^*_σ orbital which is mixed into the 26A′(12B$_1$) LUMO ground state. In addition, the increased value of $-2J$ in Table VIII for the cis dimer relative to the trans dimer is derived directly from the hydroxide p_x orbital which also mixes into the LUMO ground state (Figure 8A), providing another superexchange pathway that acts in a complementary manner to increase the magnitude of the exchange coupling. As shown in the middle column of Figure 13, the combined destabilizing interactions of the Π^*_σ and the OH p_x on the 26A′(12B$_1$) LUMO lead to a larger HOMO–LUMO splitting relative to the end-on trans dimer, 2. The peroxide Π^*_σ orbital is also the primary superexchange pathway in the side-on dimer, 5. As shown in Figure 9B, the peroxide Π^*_σ orbital contributes to the singlet-triplet splitting in 5 by acting as a donor orbital destabilizing the LUMO (last column, Figure 13). The four Cu–O σ bonding

(37) Hay, P. J.; Thibeault, J. C.; Hoffmann, R. *J. Am. Chem. Soc.* **1975**, *97*, 4884-4899.

interacttions in the side-on dimer lead to larger destabilization of the LUMO than in the end-on dimers. In addition, Figure 9C shows that the unoccupied peroxide σ^* orbital provides another orbital pathway by acting as a π acceptor orbital stabilizing the HOMO. The combined effect of the pathways through the Π^*_σ donor orbital and the unoccupied σ^* acceptor orbital leads to the largest HOMO–LUMO splitting in Figure 13 and is responsible for the very large antiferromagnetic coupling in **5**.

The ligand-to-metal charge-transfer transitions in the absorption spectrum of a copper–peroxide complex can be used as a direct measurement of the Π^*_v–Π^*_σ splitting and, therefore, provide a direct probe of the ligand–metal bonding contributions to the electronic structure. Since the Π^*_v–Π^*_σ splitting (Figure 12) has a dramatic dependence on the geometry of the copper–peroxide bond, the absorption spectrum can be used to extract geometric information. A comparison of the observed transition energies (Table IXB) of the end-on trans dimer, **2**, and the side-on dimer, **5**, reveals that the Π^*_v transition remains at relatively the same energy in both complexes, while the Π^*_σ transition is at much higher energy in the side-on dimer, leading to a much larger observed Π^*_v–Π^*_σ splitting for **5** compared to **2**, in agreement with the splittings predicted in Figure 12 and Table IXA. On the basis of the calculated transition energies and the Π^*_v–Π^*_σ splittings, the end-on cis dimer, **3**, would be expected to have an absorption spectrum similar to that of the trans dimer but shifted slightly to lower energy due to the destabilizing effect that the bridging hydroxide has on the peroxide orbitals by donating electron density onto the coppers.

The end-on cis dimer and side-on dimer structures considered in this study provide an opportunity to directly consider the two proposed models of the oxyhemocyanin active site. The binuclear copper active site in oxyhemocyanin is strongly antiferromagnetically coupled,[7] has a low O–O stretching frequency of 750 cm^{-1},[6] and has a unique absorption spectrum consisting of an intense Π^*_v charge-transfer transition at 580 nm (17 250 cm^{-1}) and a very intense Π^*_σ charge-transfer transition at 345 nm (29 000 cm^{-1}).[5] Both the end-on cis dimer, **3**, and the side-on dimer, **5**, are calculated to have large antiferromagnetically coupled ground states consistent with oxyhemocyanin. On the basis of the Π^*_v–Π^*_σ splitting and the calculated Π^*_σ transition energies, the end-on cis dimer is expected to have an absorption spectrum with an intense Π^*_σ charge-transfer transition around 14 600 cm^{-1}, whereas the Π^*_σ transition in the side-on dimer should be at higher energy, consistent with the model complex analogous to **5**. On the basis of the electron density on the oxygen atoms, the end-on cis dimer, **3**, is expected to have an O–O stretching frequency similar to that of the end-on trans dimer, **2**, which has an observed ν_{O-O} of 832 cm^{-1} for the structural analogue. Alternatively, the additional σ^* acceptor interaction in the side-on dimer, **5**, shifts electron density into a strongly antibonding MO and provides a direct explanation for the low O–O stretching frequency observed in the Raman spectrum of this model complex. In addition, both of the proposed models are consistent with the lack of observed Cu–O stretching frequencies in the resonance Raman spectrum of oxyhemocyanin, as the Π^*_σ orbital is seen to be extensively delocalized over the two coppers in both the end-on cis and side-on dimer calculations and hence is in the strong coupling limit (vide supra). However, the Π^*_σ orbital in the side-on dimer calculation (Cu = 2.60 bohr) is seen to mix with an amine N$_\sigma$ bonding level, providing an explanation for the enhancement of Cu–N stretching modes in the resonance Raman spectrum. Therefore, on the basis of these calculations, the side-on dimer, **5**, appears to be more consistent with the observed properties of oxyhemocyanin than the end-on cis dimer, **3**. However, in the absence of experimental data, either a high-resolution crystal structure of oxyhemocyanin or a structurally characterized analogue of **3**, the end-on cis dimer cannot be ruled out as a model of the oxyhemocyanin active site. The polarized absorption spectrum of single crystals of oxyhemocyanin should provide a direct experimental determination of the appropriate model for the active site structure, since the selection rules for the Π^*_σ transition in the D_{2h} side-on dimer ($^1B_{3u}$) require it to be polarized along the Cu–Cu direction, whereas the
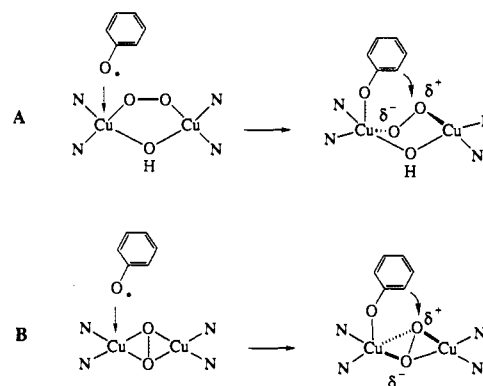

Figure 14. Proposed reaction mechanism for tyrosinase, where substrate binding causes electrophilic activation of the asymmetrically bound peroxide. (A) Reactive intermediate for the end-on cis μ-1,2 geometry. (B) Reactive intermediate for the side-on μ-η^2:η^2 geometry.

Π^*_σ transition in the C_{2v} end-on cis dimer ($^1A_1$) should be polarized along the C_2 axis which is perpendicular to the Cu–Cu direction.

Another important goal of this study is to understand how the geometry and electronic structure of copper–peroxide systems lead to reversible dioxygen binding and activation of the dioxygen toward hydroxylation of aromatic substrates. Both oxyhemocyanin and oxytyrosinase reversibly bind dioxygen and have very similar spectral features, indicating very similar geometries, bonding, and electronic structures with respect to the copper–peroxide bond. In addition to effects such as solvation and pK_a which can shift the equilibrium of dioxygen binding, the electronic structural contribution to the strength of the copper–peroxide bond is a major factor in determining stability of the copper–peroxide adduct. Therefore, it is clear that if other factors remain constant, the side-on dimer, **5**, should form a significantly more stable complex than dimer structures with a peroxide bound in an end-on geometry and complexes with the peroxide bound to a single copper having the least stable structure. This appears to be consistent with the qualitative observations on the side-on dimer, [Cu(HB(3,5-iPr$_2$pz)$_3$]$_2$(O$_2$), which appears to be more stable than the trans dimer, [(CuL)$_2$(O$_2$)]$^{2+}$, which is in turn more stable than the end-on monomer, [Cu$_2$(XYL-O-)O$_2$]$^{1+}$. The electronic contributions that stabilize the copper–peroxide complexes also influence their reactivity. In recent years, several model complexes have been synthesized which activate dioxygen and undergo similar hydroxylation chemistry to tyrosine. One characteristic of these reactions is the apparent electrophilic character of the peroxide intermediate. Three reaction mechanisms have been considered which allow the peroxide to act as an electrophilic oxidant and lead to activation of the copper–peroxide intermediate.

A reaction mechanism for tyrosinase has been proposed on the basis of an end-on cis μ-1,2 structure where the substrate binds to one copper causing a weakening of the peroxide bond to that copper.[38] Substrate binding causes the asymmetrically bound peroxide to be heterolytically polarized with more electron density located on the weakly bound oxygen atom, while the more strongly bound oxygen atom has less electron charge and is available for electrophilic attack on the substrate, as shown in Figure 14A. The electronic structure of the asymmetrically bound peroxide intermediate can be approximated by the calculation of the end-on monomer, **1** (Table VII), which places more electron density on the weakly bound oxygen atom in agreement with the proposed mechanism. A similar asymmetrically bound intermediate can be proposed for the side-on μ-η^2:η^2 geometry as shown in Figure 14B.

The second mechanism involves electronic activation of the peroxide and is related to a mechanism considered by Sorrell,[39] which involves the unoccupied peroxide σ^* orbital. Our calculations on the side-on dimer, **5**, demonstrate the importance of

(38) Wilcox, D. E.; Porras, A. G.; Hwang, Y. T.; Lerch, K.; Winkler, M. E.; Solomon, E. I. *J. Am. Chem. Soc.* **1985**, *107*, 4015–4027.

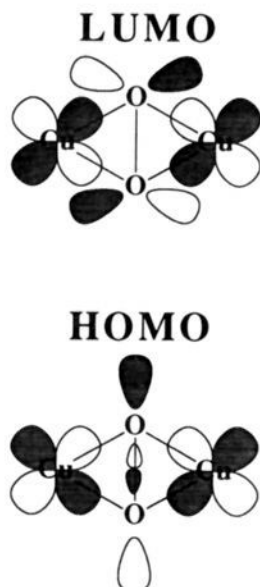(39) Sorrell, T. N. *Tetrahedron* **1989**, *45*, 3–68.

LUMO

HOMO

Figure 15. HOMO and LUMO levels of the side-on μ-η^2:η^2 dimer responsible for the electronic activation of the symmetrically bound peroxide for electrophilic attack of the substrate. Mixing of the σ^* into the HOMO weakens the O–O bond for cleavage, while Π^*_σ mixing into the LUMO donates electron density to the coppers and increases the electrophilic nature of the peroxide.

the σ^* orbital's participation in bonding. By mixing into the ground-state $9B_1$ HOMO level in Figure 15, the σ^* becomes partially occupied in the ground state, weakening the O–O bond (resulting in a low ν_{O-O}) and activating the peroxide for cleavage. In addition, compared to other peroxide binding geometries, the side-on dimer has the least negative, most electrophilic peroxide due to the four σ donor bonding interactions of Π^*_σ orbital. The combined effects of the weakened O–O bond and the increased electrophilicity of the peroxide in the side-on dimer, **5**, activate the symmetrically bound peroxide for hydroxylation of aromatic substrates. Electron donation from the substrate into the electrophilic LUMO, which has antibonding interactions between the copper and peroxide and between the oxygen atoms of the peroxide (Figure 15), would induce cleavage of both the Cu–O and O–O bonds, resulting in oxygen transfer to the substrate. The active site in tyrosinase has been determined to directly bind substrate which, as shown in Figure 14B, would orient the phenol and provide an orbital pathway for electron transfer to this lowest energy unoccupied orbital. The alternative possibility of electron donation from the substrate into the peroxide σ^* orbital is less

likely since it is calculated to be 31 860 cm^{-1} higher than the LUMO.

The third mechanism is based on Karlin's observation that some model complexes require a proton for reactivity.[40] This is the case for $[Cu_2(XYL-O-)O_2]^{1+}$, which has a terminally bound peroxide to a single copper(II) ion. In the unprotonated form, this complex does not react with triphenylphosphine, Ph_3P, but rather reacts with CO_2 and SO_2 exhibiting nucleophilic character. Indeed, the $X\alpha$ calculations on **1** support this observation, showing that the terminal oxygen atom (O2) is electron rich and has more electron density than the bound oxygen atom (O1). When $[Cu_2(XYL-O-)O_2]^{1+}$ is protonated, it is thought to form a μ-1,1 hydroperoxide complex which is electrophilic and capable of oxidizing Ph_3P to Ph_3PO.[41] The proton is expected to form a covalent bond to the peroxide, withdrawing electron density and leading to electrophilic activation of the peroxide. While this mechanism is probably not appropriate for tyrosinase, it may be important in the dopamine β-hydroxylase catalyzed benzylic hydroxylation reaction.[42]

The bonding and molecular properties of copper–peroxide complexes have their electronic structural origin in the degree of stability of the peroxide Π^*_σ orbital with respect to the nonbonding Π^*_v orbital. The primary contribution to the formation of Cu–O σ bonds involves a bonding interaction between the peroxide Π^*_σ and the Cu d ground state. This σ bonding interaction not only affects the strength of the Cu–O bond but also influences the O–O bond strength and the magnitude of the ground-state exchange interaction and determines the Π^*_v–Π^*_σ splitting observed in the absorption spectrum. The side-on dimer, **5**, is unique in that it has an additional interaction involving the unoccupied peroxide σ^* orbital acting as a π acceptor stabilizing the Cu d_{xy} HOMO. This σ^* interaction is found to significantly affect the strength of both the Cu–O bond and the O–O bond and acts to increase the magnitude of the ground-state exchange interaction.

Supplementary Material Available: Listings of energies and charge decompositions for the one-electron eigenfunctions from SCF-Xα-SW calculations on all five structures with the Norman sphere radii, with the copper sphere radii equal to 2.60 bohr, and with the copper sphere radii equal to 2.95 bohr (41 pages). Ordering information is given on any current masthead page.

(40) Tyeklar, Z.; Karlin, K. D. *Acc. Chem. Res.* **1989**, *22*, 241–248.
(41) Karlin, K. D.; Cruse, R. W.; Gultneh, Y. *J. Chem. Soc., Chem. Commun.* **1987**, 599–600.
(42) (a) Miller, S. M.; Klinman, J. P. *Biochemistry* **1985**, *24*, 2114–2127. (b) Stewart, L. C.; Klinman, J. P. *Annu. Rev. Biochem.* **1988**, *57*, 551–592.